

Scalable quantum error mitigation for dynamical decoupling

Weibin Ni^{1,2}, Zhijie Li³, Guanyu Qu³, Asif Equbal^{4,5}, Zhecheng Sun^{2,6}, Jiale Dai^{1,2},
Fazhan Shi^{3,7}, Lei Sun^{1,2,6,*}

¹Department of Physics, School of Science and Research Center for Industries of the Future, Westlake University, Hangzhou 310030, Zhejiang Province, China.

²Institute of Natural Sciences, Westlake Institute for Advanced Study, Hangzhou 310024, Zhejiang Province, China.

³Laboratory of Spin Magnetic Resonance, School of Physical Sciences, Anhui Province Key Laboratory of Scientific Instrument Development and Application, University of Science and Technology of China, Hefei 230026, China.

⁴Center for Quantum and Topological Systems, New York University Abu Dhabi, United Arab Emirates

⁵Department of Chemistry, New York University Abu Dhabi, United Arab Emirates

⁶Department of Chemistry, School of Science and Research Center for Industries of the Future, Westlake University, Hangzhou 310030, Zhejiang Province, China.

⁷School of Biomedical Engineering and Suzhou Institute for Advanced Research, University of Science and Technology of China, Suzhou 215123, China

*Corresponding author. Email: sunlei@westlake.edu.cn

Quantum coherence remains a fundamental challenge for advancing quantum technologies. Although dynamical decoupling can suppress decoherence noise, it frequently misestimates decoherence times due to control errors—a previously underappreciated issue. Here, we present Hadamard phase cycling, a scalable non-Markovian quantum error mitigation method using group-structured phase configurations to filter spurious dynamics. Validated across molecular electron spins, nitrogen-vacancy centers in diamond, nuclear spins, trapped ions, and superconducting qubits, this technique enables accurate decoherence time characterization and enhanced state fidelity with linear complexity. Our results indicate that many reported ultralong decoherence times stem from artifacts like coherence-population mixing rather than genuine noise suppression. By ensuring dynamical authenticity, Hadamard phase cycling establishes a robust framework for reliable quantum control, paving the way for reassessment and advancement of coherence benchmarks in the NISQ era.

Quantum information science holds great promise for delivering transformative computational power, metrological sensitivity, and communication security beyond classical limits (1). In the current Noisy Intermediate-Scale Quantum (NISQ) era, the realization of quantum advantages is hampered by susceptibility of qubits to decoherence and control errors (2). In principle, quantum error correction can eliminate these errors and enable fault-tolerant quantum technologies, but it imposes stringent demands on error rates and requires a substantial overhead of physical qubits—conditions that are presently beyond technological reach (3, 4).

Dynamical decoupling, which applies a pulse sequence to average out unwanted environment–system coupling, is a well established strategy to suppress the decoherence error (5–7). It has been widely applied to extend decoherence times (T_2) for versatile qubit platforms, e.g. nuclear spins (8), solid-state spin defects (9–12), neutral atoms (13), superconducting circuits (14, 15), trapped ions (16), semiconductor quantum dots (17, 18), paramagnetic molecules (19–22), etc. The capability of coherence preservation enables applications of dynamical decoupling across a wide range of quantum technologies, including Hamiltonian engineering in quantum simulation (23), noise spectrum reconstruction (24, 25), sensitive and selective quantum metrology (26), and state protection in quantum computing (27). Meanwhile, it is also widely applied in nuclear magnetic res-

onance (NMR), electron paramagnetic resonance (EPR), and magnetic resonance imaging (MRI), empowering precise measurements of spin-spin interaction as well as the fast spin echo method for efficient MRI (28).

However, dynamical decoupling itself is prone to control errors, causing accumulation of erroneous dynamic evolution of quantum states that leads to low state fidelity. Although some dynamical decoupling sequences, exemplified by CPMG and XY-8, are designed with inherent robustness to protect the fidelity of final state (29), control errors may still reduce the fidelity of intermediate states and compromise characterization of dynamic properties (30). Therefore, albeit widely used for acquiring T_2 , these robust sequences tend to misestimate T_2 under control errors. This issue, pervasive across various qubit platforms and long unresolved, would misguide qubit design and optimization (31). Moreover, control errors may introduce spurious signals in quantum sensing (32) and distort echo shapes in fast spin-echo MRI, potentially resulting in misinterpreted sensing results and erroneous medical diagnosis. Addressing these challenges demands accurate and efficient quantum error mitigation (QEM) tailored for dynamical decoupling.

Here, we show that for systems whose relaxation time (T_1) well exceeds T_2 and where single gate fidelity is relatively low, dynamical decoupling without proper mitigation of control errors tends to severely overestimate T_2 or become impractical to implement. Complete error mitigation demands exponential scaling with the circuit depth according to the selection rule of coherence-only dynamic processes, yet it can be well approximated with linear scaling by quantum circuits whose phase configurations form an abelian group. Based on this property, we design Hadamard phase cycling, the first practical QEM method for inversion-pulse-based dynamical decoupling (IDD), e.g. CP, CPMG, XY-8, XY-16, and UDD, which are widely used in quantum information science and magnetic resonance spectroscopy. Applying this protocol to IDD enables accurate measurement and significant enhancement of T_2 for ensemble molecular electron spin qubits, nitrogen-vacancy (NV) centers in diamond, and nuclear spin qubits. Benchmarking it on single trapped $^{40}\text{Ca}^+$ ion and superconducting transmon qubits yields near-quantitative effective state fidelity.

Results

Practical phase cycling for IDD

QEM is a highly feasible strategy to handle control errors of pulses (i.e. single quantum gates) (33, 34). By post-processing outputs from an ensemble of noisy quantum circuits, QEM reduces the impact of errors and more accurately estimates expectation values of observables. Phase cycling, which was developed decades ago in the context of NMR and then extended to EPR (35), MRI (36), and optical spectroscopy (37), is likely the first QEM method. Typically, phase cycling employs a set of functionally equivalent quantum circuits (i.e. pulse sequences) leveraging their phase degree of freedom. The phase configurations are systematically designed by classifying qubit dynamics based on their evolution pathways (38). This approach selectively extracts the desired dynamics by averaging observables obtained from all circuits. Hence, phase cycling is a non-Markovian QEM yet both its potential in quantum information science and its application for dynamical decoupling have remained largely unexplored.

We consider a qubit in a dephasing environment under IDD with systematic control errors (Fig. 1A). Rapid environmental fluctuations beyond the refocusing capability of the control pulses are captured as an exponential decay. To describe the resulting qubit dynamics, the quantum state is decomposed into coherence orders $p \in \{0, \pm 1\}$, where $p = \pm 1$ represents transverse coherence subject to decoherence and $p = 0$ denotes longitudinal population subject to relaxation. Each control pulse acts as a branch point (Fig. 1E), redistributing these orders with weights determined by control imperfections. Consequently, a multi-pulse sequence generates an exponentially vast manifold of coherence transfer pathways, each encoding distinct non-Markovian dynamics.

Reliable implementation of phase cycling could construct an effective quantum channel that selectively isolates the target dynamics from spurious pathways. However, most previous studies implemented IDD without phase cycling or with two-step phase cycling (TPC). TPC suffices to select desired dynamic processes only when all pulses are error-free, whereas noisy inversion pulses induce unintended coherence-order changes ($\Delta p = \pm 1$) and cause coherence-population mixing (Fig. 1B and E). The pathways consisting of only $p = \pm 1$ states generate desired signals reflecting pure decoherence; those involving $p = 0$ states generate undesired signals that undergo intermittent relaxation processes. To illustrate this point, we applied a modified CPMG sequence

on an ensemble of Cu^{2+} -based molecular qubits (Fig. 2B inset) to separate desired and undesired spin echoes (Fig. 1C) (39). The former decays more than 600 times faster than the latter (Fig. 1D). In standard CPMG experiments, these two types of echoes overlap, causing TPC to overestimate T_2 that leads to positively biased thereby misleading assessment of qubit performance.

Rigorous QEM for IDD requires precise isolation of coherence-only dynamic processes. In an IDD- m sequence, imperfections in any combination of the m pulses can trigger transitions between coherence and population. Consequently, the signal becomes a superposition of desired decoherence pathways and an exponentially large manifold of spurious pathways involving relaxation (2^m possibilities). We extract the former by exploiting the phase degree of freedom: applying a π phase shift to a pulse inverts the sign of any signal whose corresponding pathway involves an error at that pulse (Fig. 1C). Accordingly, we represent a pulse phase by a binary basis $\{\pm 1\}$, where $+1$ denotes the original phase and -1 denotes a π phase shift. In theory, eliminating undesired signals requires summing over a complete basis of phase configurations for all pulses—a method termed as complete phase cycling (CPC) (19, 31, 40). However, CPC demands 2^m distinct quantum circuits (supplementary material), rendering it unscalable for deep circuits.

We surmount this exponential barrier by approximating the filtering power of CPC while implementing linear scaling. Mathematically, phase configurations forming an abelian group ensure destructive interference and vanishment of most erroneous pathways upon averaging. Accordingly, we design phase configurations using Sylvester-constructed Hadamard matrices (41), i.e. square matrix whose columns form an abelian group under Hadamard product, and integrate them with a parity-based selection rule, yielding the Hadamard phase cycling (HPC) protocol (Fig. S1; see details in the supplementary material):

$$HPC = \begin{pmatrix} + & +\vec{1}_m & +\vec{1}_m & +H' \\ + & +\vec{1}_m & +\vec{1}_m & -H' \\ - & -\vec{1}_m & +\vec{1}_m & +H' \\ - & -\vec{1}_m & +\vec{1}_m & -H' \end{pmatrix}. \quad (1)$$

Here, the columns represent the phase settings for all pulses across different quantum circuits, $\vec{1}_m$ is an all-ones vector of size m , H' is a Sylvester-constructed Hadamard matrix excluding the first column, and the sign column dictates the data processing (addition or subtraction). For a sequence

of length m (where m is a power of 2 for simplicity), HPC reduces the complexity from 2^m to $4m$ while retaining near-quantitative error mitigation—it filters more than 98% erroneous pathways for $m > 16$ (Fig. S2). Thus, HPC transforms a theoretically intractable problem into a scalable experimental strategy (Fig. 2A).

Quantum error mitigation for ensemble qubits

The non-Markovian nature of HPC enables its application for accurate T_2 acquisition. As proof of concept, we implemented Hadamard, complete, and two-step phase cycling for CPMG- m to acquire T_2 of the ensemble Cu^{2+} -based molecular qubit (Fig. 2B inset) with pulse EPR spectroscopy. We first fixed the delay time between adjacent pulses while increasing the number of pulses. Hadamard and complete phase cycling yielded nearly identical echo intensities for each sequence with $m = 2 - 16$ (Fig. 2B). This phenomenon reinforces the nearly quantitative error mitigation of HPC and shows the advantage of its linear scalability: for $m = 16$, HPC exerts 64 quantum circuits while CPC demands 65536 circuits. In sharp contrast, TPC leads to a much slower echo decay with increasing m , giving rise to significantly stronger echoes (Fig. 2B). This indicates substantial coherence-population mixing—TPC on noisy quantum circuits does not probe pure decoherence and more reliable phase cycling are indispensable to mitigate control errors.

The distinction between two-step and Hadamard phase cycling becomes critical when measuring T_2 with fixed number of pulses and variable delay times. Both methods exhibit an increase of the apparent T_2 with increasing sequence length, yet they display drastically different scaling factors: $T_2 \propto m^{0.42}$ for TPC and $T_2 \propto m^{0.17}$ for HPC (Fig. 2C). CPMG with TPC requires 256 pulses to improve T_2 by more than 10 times, whereas HPC would enforce nearly 0.9 million pulses should its scaling law be applicable to longer sequences. From another perspective, TPC would overestimate T_2 by an order of magnitude for CPMG-8192. Under proper error mitigation provided by HPC, CPMG-128 improves T_2 to 24 μs , approximately four times of the value obtained from Hahn echo decay (Fig. S3), demonstrating utility of dynamical decoupling for coherence protection. Similar behavior were observed for ensemble radical-based molecular qubits embedded in a covalent organic framework (42) and nuclear spins of ^1H in ^{13}C -labelled glycine (Fig. S4 and S5).

We observed similar phenomena in another representative ensemble electron spin qubit system,

i.e. NV centers in diamond (Fig. 2D inset). For CPMG- m experiments with fixed delay time, the echo intensity decays much faster under HPC than TPC as m increases (Fig. 2D). For those with fixed sequence length and variable delay time, TPC gives rise to longer apparent T_2 than HPC for CPMG-32 and CPMG-64 (Fig. S6). Remarkably, employing CPMG-1536 with TPC yields an apparent T_2 approaching $0.25T_1$, indicating that such a long sequence mixes decoherence with relaxation (Fig. 2E). Overall, these experiments confirm that although TPC generates seemingly more promising coherence enhancement, it inevitably involves coherence-population mixing and causes significant overestimation of T_2 . HPC, which balances effectiveness and scalability for error mitigation, provides a practical solution for T_2 acquisition of ensemble qubit systems.

HPC is also applicable to UDD, which is theoretically the optimal dynamical decoupling sequence under pure-dephasing model (43, 44) (Fig. 3A). For the Cu^{2+} -based molecular qubits, complete and Hadamard phase cycling again yielded well-defined echoes with identical intensities for UDD- m with $m = 2 - 10$ (Fig. 3B). In contrast, TPC generated complex echo signals with wrong phases likely due to overlapping of desired echoes with undesired ones (Fig. 3B inset). UDD- m with HPC shows $T_2 \propto m^{0.81}$ (Fig. 3C). The scaling factor is much larger than that of CPMG- m with HPC (0.17), demonstrating much better performance of UDD- m for decoherence error suppression. Specifically, UDD-8 slightly outperforms CPMG-64 (Fig. 3D), and UDD-14 improves T_2 to $35 \mu\text{s}$ that well exceeds the value observed for CPMG-128 ($T_2 = 24 \mu\text{s}$). Clearly, UDD is significantly undermined by control errors under TPC, which could prevent its correct implementation under noisy hardware and lead to misinterpretation and underestimation of its performance on decoherence error suppression. Thus, quantum error mitigation, exemplified by HPC, is indispensable for reliable evaluation of dynamical decoupling sequences. The effectiveness of HPC on the robust, periodic CPMG and non-robust, aperiodic UDD proves that it is generally applicable to IDD. Such a universality provides HPC with extensive applications, ranging from rational design of dynamical decoupling sequences to quantum sensing and fast spin-echo MRI (26, 28).

Quantum error mitigation for single qubits

To quantify the performance of phase cycling on single-qubit platforms, we introduce the effective state fidelity (F^{eff}). Because phase cycling averages the outputs of multiple quantum circuits prone

to control and decoherence errors, the resulting state is fundamentally a mixed state. We therefore normalize the averaged state to its pure-state equivalent ρ , which effectively decouples the control-error mitigation performance from the irreversible decoherence. This normalized state ρ is then compared to the ideal target state σ using the standard fidelity metric:

$$F^{eff} = (Tr \sqrt{\sqrt{\rho}\sigma\sqrt{\rho}})^2. \quad (2)$$

We experimentally benchmarked TPC and HPC on single trapped ion and superconducting qubits with CP- m and UDD- m sequences that lack inherent robustness. The final state of each quantum circuit was characterized by quantum state tomography. For CP- m with 2 – 16 inversion pulses exerted on single trapped $^{40}\text{Ca}^+$ ion qubit, HPC retains F^{eff} above 99.5% (Fig. 4C). In sharp contrast, the fidelity quickly declines to 58.3% for CP-16 with TPC. This trend was reproduced by UDD- m , where F^{eff} is 99.5% on UDD-64 with HPC yet it plummets to 15.0% with TPC (Fig. 4D). Single superconducting transmon qubit exhibits similar behaviors, with TPC significantly deteriorating the effective state fidelity while HPC maintains remarkable robustness under relatively large systematic error (Fig. S7 and S8).

The key advantage of HPC lies in its ability to separate the qubit’s population and coherence, mimicking an ideal inversion pulse. It is evidenced by negligible z-component in the effective state (Fig. 4A), which is in stark contrast to the salient z-component observed in the final state of each individual quantum circuit (Fig. 4B and Fig. S8). Therefore, given a relatively low single gate fidelity, dynamical decoupling itself is prone to erroneous dynamic evolution of intermittent states. HPC can mitigate the control error for every intermittent state, allowing reliable dynamical decoupling. As dynamical decoupling is routinely used to protect quantum information of idle qubits during quantum algorithms (3), its integration with scalable phase cycling could improve the performance of quantum computing.

Discussion

By leveraging the phase degree of freedom in quantum circuits and the abelian group structure, we designed Hadamard phase cycling as the first practical non-Markovian quantum error mitigation for inversion-pulse-based dynamical decoupling. This method balances effectiveness with scalability,

enabling accurate measurement of T_2 and reliable implementation of dynamical decoupling with linear scaling for multiple leading qubit platforms.

More fundamentally, our results expose a long-standing paradox in quantum control: the “apparent” extension of T_2 often stems from spurious control-induced dynamics like coherence-population mixing rather than a genuine suppression of environmental noise. Consequently, our findings suggest that many ultralong decoherence times reported in the literature may be significantly overestimated, necessitating a community-wide re-evaluation of these benchmarks. While quantum error mitigation is indispensable for tasks inherently sensitive to the evolution history of qubits, e.g. NV-center-based nuclear magnetic resonance, Hamiltonian engineering, or qubit characterization—it is not universally mandatory. It may be omitted in scenarios where single-qubit gate fidelities are sufficiently high, or for applications that rely solely on the fidelity of the final state, provided that alternative verification methods can confirm the reliability of the implementation, e.g. quantum tomography in quantum computing.

Ultimately, these insights shift the focus of T_2 benchmarking toward task-specificity and dynamical authenticity. Furthermore, our study demonstrates that the utility of quantum error mitigation and suppression depends on a strategic balance of complexity and effectiveness. This integrated paradigm ensures that quantum control remains both scalable and physically grounded, offering new avenues for navigating the NISQ era and beyond.

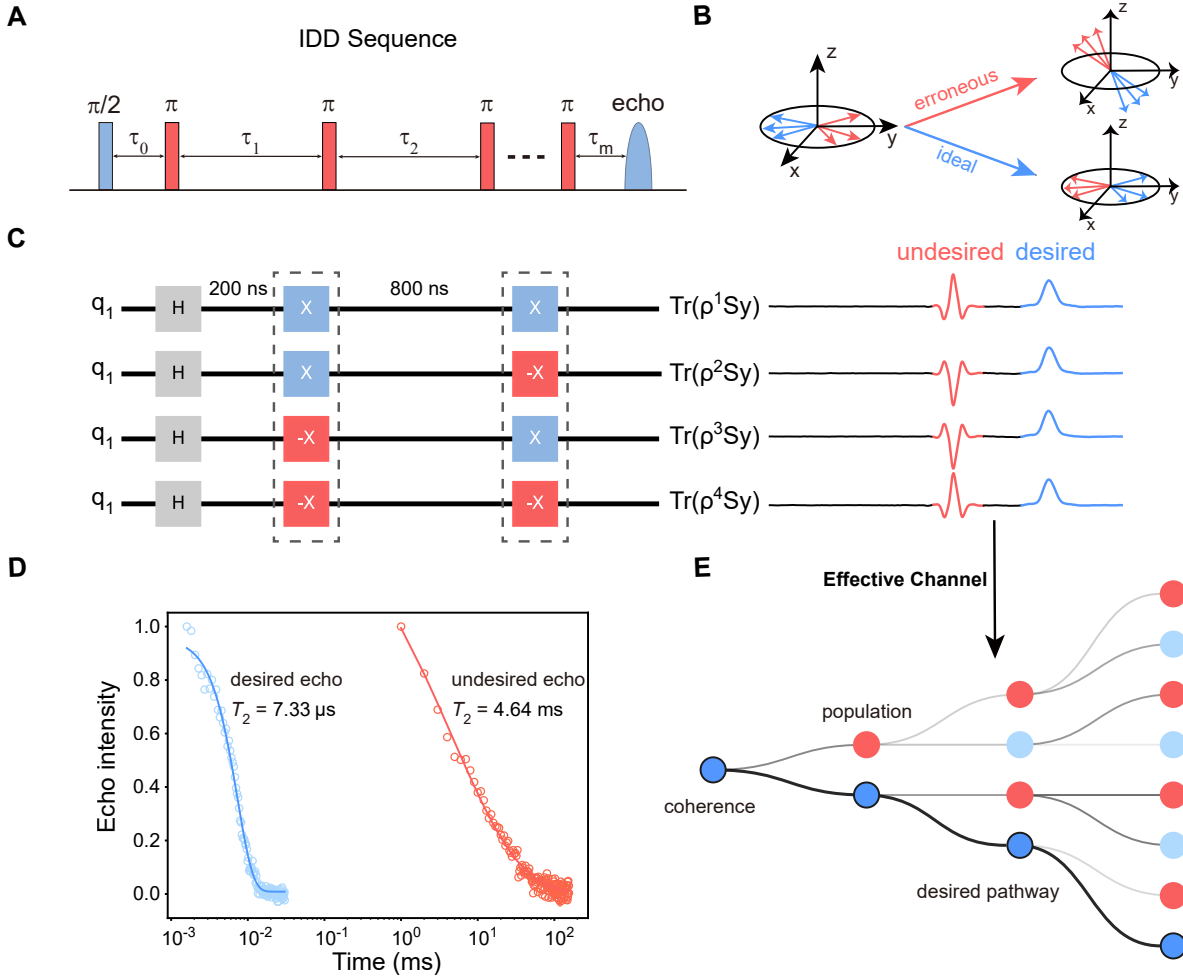


Figure 1: Introduction to phase cycling. (A), Composition of a general IDD sequence. For the CPMG sequence, the π pulses are applied at constant time intervals. Each π pulse has a phase that differs by $\pi/2$ from the phase of the initial $\pi/2$ pulse. (B), Illustrative figure of desired and undesired dynamical processes of qubits under noisy IDD sequence. (C), CPC for modified CPMG-2. q_1 and H represent qubit and Hadamard gate, respectively. $\pm X$ represent inversion pulses with opposite phases. $Tr(\rho^i S_y)$ represents the expectation value of S_y in the final state ρ^i of the i^{th} quantum circuit. Schemes on right are experimental outputs of quantum circuits with desired and undesired echoes highlighted. (D), Echo decay curves of desired and undesired echoes. Data were collected for ensemble Cu^{2+} -based molecular qubits at 8 K by varying the interval between two inversion pulses. The desired and undesired echoes decay with apparent T_2 of $7.33 \mu\text{s}$ and 4.64 ms , respectively. (E), This branching tree illustrates the exponential proliferation of coherence transfer pathways, where each imperfect control pulse redistributes the quantum state between coherence (blue) and population (red) manifolds. Reliable phase cycling selects desired coherence-only pathways.

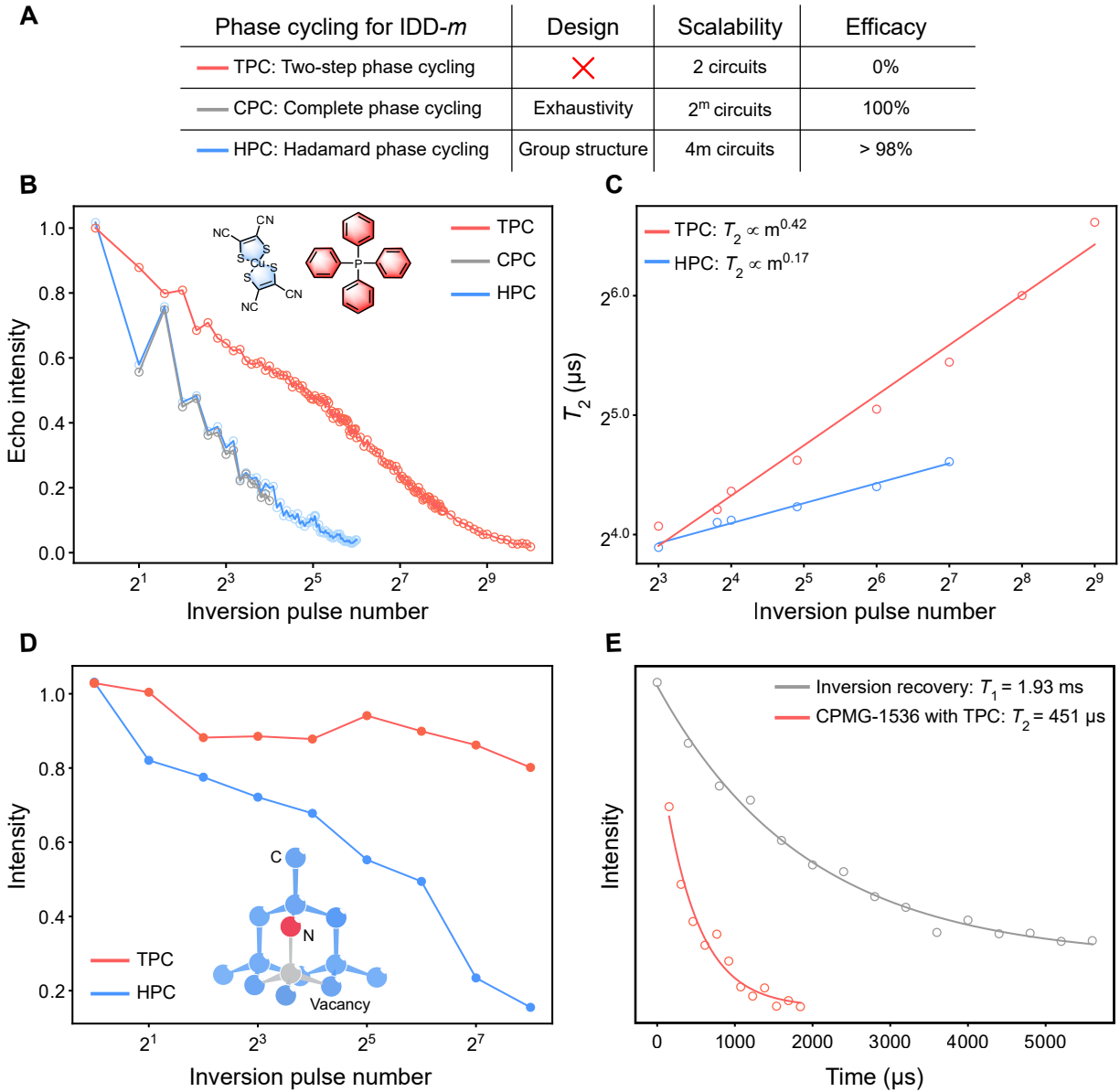


Figure 2: T_2 measurements for ensemble electron spin qubits under CPMG. (A), Introduction of different phase cycling methods. Assume that m is a power of 2 and $m > 16$ for which CPC becomes impractical. (B), Comparison of echo intensities collected with HPC, CPC, and TPC. Inset: Schematic illustrations of the Cu^{2+} -based molecular qubit. (C), Dependencies of T_2 on the number of inversion pulses for HPC and TPC. Data in (B) and (C) were collected on ensemble Cu^{2+} -based molecular qubits at 8 K. (D), Comparison of echo intensities collected with HPC and TPC. Inset: Schematic illustrations of NV center in diamond. (E), Inversion recovery curve and echo decay curve under CPMG-1536 with TPC. Data in (D) and (E) were collected on ensemble NV centers in diamond at room temperature. The x-axes of (B)-(D) and y-axis of (C) are in log scale.

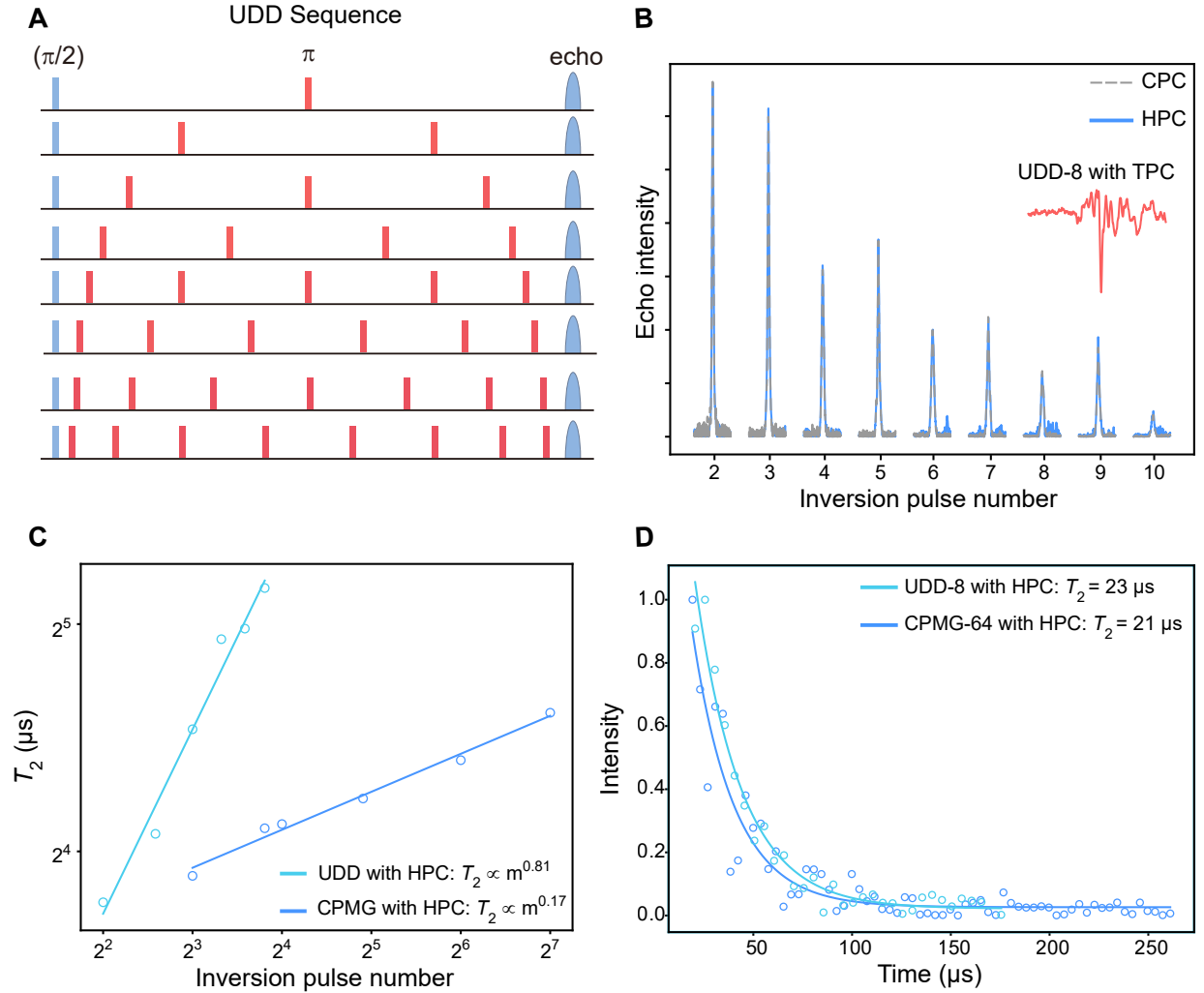


Figure 3: Application of HPC for UDD on ensemble molecular qubits. (A), Schematic illustrations of UDD-1 to UDD-8. (B), Comparison of echo intensities collected with HPC and CPC. Inset: Echo signals observed for UDD-8 with TPC. (C), Dependencies of T_2 on the number of inversion pulses for UDD and CPMG with HPC. Both axes are in log scale. (D), Comparison of echo decay curves under UDD-8 and CPMG-64 with HPC. Data were collected on ensemble Cu^{2+} -based molecular qubits at 8 K.

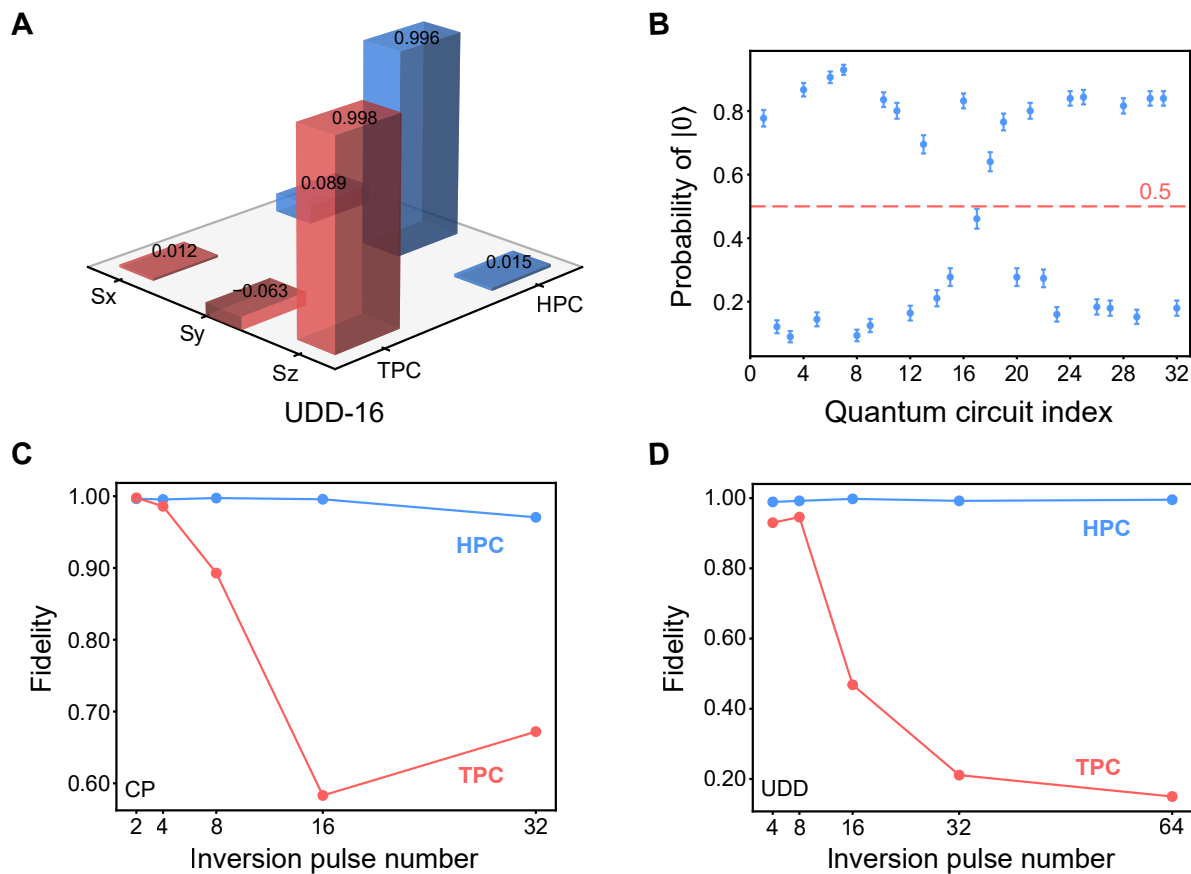


Figure 4: HPC and effective state-fidelity tests on single trapped $^{40}\text{Ca}^+$ ion qubit. (A), Quantum state tomography results of effective final states. (B), Probability of being at $|0\rangle$ state for the final state of each quantum circuit. The average of all states is 0.508, indicating nearly-zero z-component for the effective final state. (C, D), Effective state fidelity under (C) CP and (D) UDD with HPC and TPC.

References and Notes

1. D. P. DiVincenzo, Thirty years of quantum computing. *Quantum Science and Technology* **10** (3), 030501 (2025), doi:10.1088/2058-9565/ade0e4.
2. J. Preskill, Quantum computing in the NISQ era and beyond. *Quantum* **2**, 79 (2018), doi:10.22331/q-2018-08-06-79.
3. G. Q. AI, Collaborators, Quantum error correction below the surface code threshold. *Nature* **638** (8052), 920–926 (2025), doi:10.1038/s41586-024-08449-y.
4. Y. Kim, *et al.*, Evidence for the utility of quantum computing before fault tolerance. *Nature* **618** (7965), 500–505 (2023), doi:10.1038/s41586-023-06096-3.
5. P. C. Maurer, *et al.*, Room-temperature quantum bit memory exceeding one second. *Science* **336** (6086), 1283–1286 (2012), doi:10.1126/science.1220513.
6. H. Zhou, *et al.*, Quantum metrology with strongly interacting spin systems. *Physical Review X* **10** (3), 031003 (2020), doi:10.1103/physrevx.10.031003.
7. D. Suter, G. A. Álvarez, Colloquium: Protecting quantum information against environmental noise. *Reviews of Modern Physics* **88** (4), 041001 (2016), doi:10.1103/revmodphys.88.041001.
8. S. Meiboom, D. Gill, Modified spin-echo method for measuring nuclear relaxation times. *Review of Scientific Instruments* **29** (8), 688–691 (1958), doi:10.1063/1.1716296.
9. G. de Lange, Z. H. Wang, D. Ristè, V. V. Dobrovitski, R. Hanson, Universal dynamical decoupling of a single solid-state spin from a spin bath. *Science* **330** (6000), 60–63 (2010), doi:10.1126/science.1192739.
10. W. K. Schenken, *et al.*, Long-lived coherences in strongly interacting spin ensembles. *Physical Review A* **110** (3), 032612 (2024), doi:10.1103/physreva.110.032612.
11. P. Siyushev, *et al.*, Coherent properties of single rare-earth spin qubits. *Nature Communications* **5** (1), 3895 (2014), doi:10.1038/ncomms4895.

12. N. Bar-Gill, L. Pham, A. Jarmola, D. Budker, R. Walsworth, Solid-state electronic spin coherence time approaching one second. *Nature Communications* **4** (1), 1743 (2013), doi: 10.1038/ncomms2771.
13. C. H. Chow, B. L. Ng, C. Kurtsiefer, Coherence of a dynamically decoupled single neutral atom. *Journal of the Optical Society of America B* **38** (2), 621 (2021), doi:10.1364/josab.413411.
14. B. Pokharel, N. Anand, B. Fortman, D. A. Lidar, Demonstration of fidelity improvement using dynamical decoupling with superconducting qubits. *Physical Review Letters* **121** (22), 220502 (2018), doi:10.1103/physrevlett.121.220502.
15. N. Ezzell, B. Pokharel, L. Tewala, G. Quiroz, D. A. Lidar, Dynamical decoupling for superconducting qubits: A performance survey. *Physical Review Applied* **20** (6), 064027 (2023), doi:10.1103/physrevapplied.20.064027.
16. P. Wang, *et al.*, Single ion qubit with estimated coherence time exceeding one hour. *Nature Communications* **12** (1), 233 (2021), doi:10.1038/s41467-020-20330-w.
17. M. Veldhorst, *et al.*, An addressable quantum dot qubit with fault-tolerant control-fidelity. *Nature Nanotechnology* **9** (12), 981–985 (2014), doi:10.1038/nnano.2014.216.
18. E. J. Connors, J. Nelson, L. F. Edge, J. M. Nichol, Charge-noise spectroscopy of Si/SiGe quantum dots via dynamically-decoupled exchange oscillations. *Nature Communications* **13** (1), 940 (2022), doi:10.1038/s41467-022-28519-x.
19. J. Du, *et al.*, Preserving electron spin coherence in solids by optimal dynamical decoupling. *Nature* **461** (7268), 1265–1268 (2009), doi:10.1038/nature08470.
20. Y. Dai, *et al.*, Experimental protection of the spin coherence of a molecular qubit exceeding a millisecond. *Chinese Physics Letters* **38** (3), 030303 (2021), doi:10.1088/0256-307x/38/3/030303.
21. J. S. Feder, *et al.*, A fluorescent-protein spin qubit. *Nature* **645** (8079), 73–79 (2025), doi: 10.1038/s41586-025-09417-w.

22. S. H. Hansen, *et al.*, Probing decoherence in molecular 4f qubits. *Chemical Science* **15** (48), 20328–20337 (2024), doi:10.1039/d4sc05304d.
23. W. Morong, *et al.*, Engineering dynamically decoupled quantum simulations with trapped ions. *PRX Quantum* **4** (1), 010334 (2023), doi:10.1103/prxquantum.4.010334.
24. G. A. Álvarez, D. Suter, Measuring the spectrum of colored noise by dynamical decoupling. *Physical Review Letters* **107** (23), 230501 (2011), doi:10.1103/physrevlett.107.230501.
25. J. Bylander, *et al.*, Noise spectroscopy through dynamical decoupling with a superconducting flux qubit. *Nature Physics* **7** (7), 565–570 (2011), doi:10.1038/nphys1994.
26. Z. Zhao, *et al.*, Sub-nanotesla sensitivity at the nanoscale with a single spin. *National Science Review* **10** (12), nwad100 (2023), doi:10.1093/nsr/nwad100.
27. H. K. Ng, D. A. Lidar, J. Preskill, Combining dynamical decoupling with fault-tolerant quantum computation. *Physical Review A* **84** (1), 012305 (2011), doi:10.1103/physreva.84.012305.
28. J. P. Mugler, Optimized three-dimensional fast-spin-echo MRI. *Journal of Magnetic Resonance Imaging* **39** (4), 745–767 (2014), doi:10.1002/jmri.24542.
29. A. M. Souza, G. A. Alvarez, D. Suter, Robust dynamical decoupling. *Philosophical Transactions of the Royal Society A: Mathematical, Physical and Engineering Sciences* **370** (1976), 4748–4769 (2012), doi:10.1098/rsta.2011.0355.
30. G. Mitrikas, R. Giourtsidou, Measuring reliable electron spin coherence times with dynamical decoupling sequences that use selective mw pulses. *Journal of Magnetic Resonance* **381**, 107981 (2025), doi:10.1016/j.jmr.2025.107981.
31. F. Lombardi, *et al.*, Dynamical nuclear decoupling of electron spins in molecular graphenoid radicals and biradicals. *Physical Review B* **101** (9), 094406 (2020), doi:10.1103/physrevb.101.094406.
32. M. Loretz, *et al.*, Spurious Harmonic Response of Multipulse Quantum Sensing Sequences. *Physical Review X* **5** (2), 021009 (2015), spurious harmonic response, doi:10.1103/physrevx.5.021009.

33. Z. Cai, *et al.*, Quantum error mitigation. *Reviews of Modern Physics* **95** (4), 045005 (2023), doi:10.1103/revmodphys.95.045005.
34. A. Zhang, *et al.*, Demonstrating quantum error mitigation on logical qubits. *Nature Communications* (2025), doi:10.1038/s41467-025-67768-4.
35. C. Gemperle, G. Aebli, A. Schweiger, R. Ernst, Phase cycling in pulse EPR. *Journal of Magnetic Resonance* **88** (2), 241–256 (1990), doi:10.1016/0022-2364(90)90181-8.
36. F. Ong, J. Y. Cheng, M. Lustig, General phase regularized reconstruction using phase cycling. *Magnetic Resonance in Medicine* **80** (1), 112–125 (2018), doi:10.1002/mrm.27011.
37. S. Yan, H.-S. Tan, Phase cycling schemes for two-dimensional optical spectroscopy with a pump–probe beam geometry. *Chemical Physics* **360** (1-3), 110–115 (2009), doi:10.1016/j.chemphys.2009.04.019.
38. G. Bodenhausen, H. Kogler, R. Ernst, Selection of coherence-transfer pathways in NMR pulse experiments. *Journal of Magnetic Resonance* **213** (2), 276–294 (1983), doi:10.1016/j.jmr.2011.08.033.
39. K. Bader, *et al.*, Room temperature quantum coherence in a potential molecular qubit. *Nature Communications* **5** (1), 5304 (2014), doi:10.1038/ncomms6304.
40. J. Soetbeer, L. F. Ibáñez, Z. Berkson, Y. Polyhach, G. Jeschke, Regularized dynamical decoupling noise spectroscopy – a decoherence descriptor for radicals in glassy matrices. *Physical Chemistry Chemical Physics* **23** (38), 21664–21676 (2021), doi:10.1039/d1cp03103a.
41. J. Sylvester, LX. Thoughts on inverse orthogonal matrices, simultaneous signsuccessions, and tessellated pavements in two or more colours, with applications to Newton’s rule, ornamental tile-work, and the theory of numbers. *The London, Edinburgh, and Dublin Philosophical Magazine and Journal of Science* **34** (232), 461–475 (1867), doi:10.1080/14786446708639914.
42. Z. Sun, *et al.*, Ultralong room-temperature qubit lifetimes of covalent organic frameworks. *Journal of the American Chemical Society* **147** (35), 31930–31939 (2025), doi:10.1021/jacs.5c09638.

43. W. Yang, R.-B. Liu, Universality of Uhrig dynamical decoupling for suppressing qubit pure dephasing and relaxation. *Physical Review Letters* **101** (18), 180403 (2008), doi:10.1103/physrevlett.101.180403.
44. G. S. Uhrig, Keeping a quantum bit alive by optimized π -pulse sequences. *Physical Review Letters* **98** (10), 100504 (2007), doi:10.1103/physrevlett.98.100504.

Acknowledgments

W.N. and L.S. acknowledge CIQTEK Co., Ltd., Quantum Inspire, and the Instrumentation and Service Center for Molecular Sciences at Westlake University for facility support and technical assistance. W.N. and L.S. acknowledge Dr. Zhifu Shi for providing the Cu^{2+} -based molecular qubit, Qian Cao for preliminary theoretical studies, Junfeng Wu, Dr. Zhichao Liu, and Dr. Mengxiang Zhang for assistance with experiments on trapped ion qubits, Marios Samiotis from Dicarolo laboratory for assistance with experiments on superconducting transmon qubits, and Dr. Maria Grazia Concilio and Prof. Xueqian Kong for preliminary simulations. W.N. acknowledges Dr. Aimei Zhou and Zhiyang Wang for assistance with pulse EPR spectroscopy, Jiaqi Han, Prof. Jian Li, and Prof. Huayi Chen for helpful discussions, and Yingchao Wang and Xiaoqing Yuan for assistance with artistic design. L.S. acknowledges Prof. Tijana Rajh, Dr. Tianxing Zheng, Prof. Dafei Jin, Prof. Xinhao Li, Dr. Ralph T. Weber, Dr. Yutian Wen and Prof. Lorenza Viola for helpful discussions.

Funding: This work was supported by the National Natural Science Foundation of China (grant No. 22273078, No. 92576117, and No. T2125011), the Hangzhou Municipal Funding Team of Innovation (TD2022004), and the Chinese Academy of Sciences (grant No. YSBR-068).

Author contributions: L.S. and W.N. conceived the idea, designed experiments, and oversaw the project. W.N. conducted theoretical analysis, proposed HPC and its benchmark, and performed experiments on trapped ion, superconducting, and molecular qubits. Z.L., G.Q., and F.S. performed experiments on NV centers in diamond, and W.N. assisted with these experiments. A.E. performed experiments on nuclear spins with solid-state NMR. Z.S. synthesized radical-based molecular

qubits. J.D. assisted with theoretical analysis. W.N. and L.S. co-wrote the manuscript. All authors have given approval to the final version of the manuscript.

Competing interests: There are no competing interests to declare.

Data and materials availability: The data supporting our findings are included in the article and supplementary files. Additional data generated during the study are available from the corresponding author upon request.

Supplementary materials

Materials and Methods

Supplementary Text

Figs. S1 to S8

Tables S1 to S6

Supplementary Materials for

Scalable quantum error mitigation for dynamical decoupling

Weibin Ni, Zhijie Li, Guanyu Qu, Asif Equbal, Zhecheng Sun, Jiale Dai, Fazhan Shi, Lei Sun*

*Corresponding author. Email: sunlei@westlake.edu.cn

This PDF file includes:

Materials and Methods

Supplementary Text

Figures S1 to S8

Tables S1 to S6

Materials and Methods

Ensemble electron spin qubits in molecules

(PPh₄)₂[Cu(mnt)]₂: The molecular electron spin qubit, (PPh₄)₂[Cu(mnt)₂], was synthesized following literature procedure (39). It was diluted in a diamagnetic isostructural host (PPh₄)₂Ni(mnt)₂ with a concentration of 0.3% via co-crystallization. This molecule exhibits $T_1 = 37.03$ ms and $T_2^{Hahn} = 6.54$ μ s revealed by inversion recovery and Hahn echo decay experiments, respectively. Pulse electron paramagnetic resonance (EPR) spectroscopic characterization of this molecule was performed with resonant frequency of 9.6623 GHz under 3340 G magnetic field at 8 K.

COF-5: COF-5 was synthesized from 2,3,6,7,10,11-hexahydroxytriphenylene and benzene-1,4-diboronic acid based on the literature procedure (42). It hosts semiquinone-like radical qubits derived from partially oxidation of the former linker. It exhibits decent spin dynamic properties at room temperature with 359 μ s and $T_2 = 1.3$ μ s. Pulse EPR spectroscopic characterization of this molecule was performed with resonant frequency of 9.6776 GHz under 3350.5 G magnetic field at 80 K.

Solid-State NMR (SSNMR)

¹³C nuclear spin in a labeled glycine was used as qubit for measurements, with $T_1 = 12$ s and $T_2^{Hahn} = 8573$ μ s. The sample was purchased from cambridge isotopes, and packed into a 1.3 mm zirconia rotor for magic-angle spinning (MAS) experiments. All SSNMR measurements were performed on a 14.4 T (600 MHz), wide-probe, spectrometer, using a 1.3 mm HXY fast MAS probe. The probe was shimmed using adamantane. The X-channel was tuned to ¹³C at a frequency of approximately 150 MHz. The sample was spun at the magic angle with a spin rate of 60 kHz to attenuate coherence dephasing effect from the first order chemical shift and the dipolar coupling anisotropy.

To prevent interference between the radiofrequency (rf) pulses and the spatial rotation of the sample, all refocusing pulses were synchronized with the rotor spinning. For CPMG experiments, the T_2 dephasing profile was obtained by varying the number of π pulses, with each pulse spaced by $n\tau_r$, where n was fixed at 200 and τ_r corresponded to the duration of a single rotation cycle. Following the protocol described in the main text, HPC was applied to the ¹³C channel to mitigate control

errors and isolate pure coherence pathways. Measurements were also performed using standard two-step phase cycling to benchmark the effectiveness of HPC in preventing T_2 overestimation due to coherence-population mixing.

Similar to the EPR experiments on molecular spins, nuclear spin qubits in the solid state are susceptible to control-induced artifacts. By using a high MAS rate of 60 kHz and rotor-synchronized pulses, we ensure that the T_2 measurements reflect the intrinsic decoherence of the ^{13}C spins under the applied dynamical decoupling sequences.

Ensemble electron spin qubits in diamond NV centers

The ensemble NV centers were created by implanting $^{15}\text{N}^+$ ions at an energy of 10 keV, and a dose of $5 \times 10^{12} \text{ cm}^{-2}$. The mean depth of implanted ions is approximately 30 nm. At this depth, the NV centers are sufficiently shielded from surface-induced noise and exhibit spin dynamic properties similar to those of deep NV centers. Prior to experiments, the diamond sample was chemically cleaned in a hot tri-acid mixture ($\text{H}_2\text{SO}_4 : \text{HNO}_3 : \text{HClO}_4 = 1 : 1 : 1$ by volume) at 453K. At room temperature, this sample exhibits $T_1 = 1.93 \text{ ms}$ and $T_2^{\text{Hahn}} = 9.29 \mu\text{s}$.

Trapped ion qubits

Experiments on trapped ion qubits were conducted on the CIQTEK's Ion I Quantum Computer, where each $^{40}\text{Ca}^+$ ion was confined in a segmented-blade Paul trap. The qubit was manipulated on the 729 nm optical transition at room temperature, with single-qubit gate fidelity being approximately 0.999. The relaxation time was measured to be $T_1 = 1.0 \text{ s}$ using the inversion recovery technique. The coherence time was $T_2^{\text{Hahn}} = 976 \mu\text{s}$ obtained from Hahn echo decay experiments.

Superconducting qubits

Experiments on superconducting transmon qubits were conducted on the Quantum Inspire's Starmon-7 Superconducting Quantum Processor, which consists of seven transmon qubits and is available on the cloud. Each transmon qubit was controlled via dedicated microwave and flux-bias lines for single-qubit and two-qubit gates, and was read out via a dispersively coupled resonator. Each resonator incorporated a Purcell filter and was frequency-multiplexed onto one of

two shared feedlines: one for qubits Q_0 and Q_2 , and another for the rest. More detailed information about hardwares of Starmon-7 can be found in https://github.com/DiCarloLab-Delft/QuantumInspireUtilities/blob/main/Starmon7_FactSheet.pdf. During our experiments, the single gate fidelity was well above 99%. Detailed information about the processors performance can be found on <https://monitoring.qutech.support/public-dashboards/7171f0e3cfc44995a97dff9001c4d7d1?orgId=1&from=now-7d&to=now>.

Pulse EPR spectroscopy

X-band (around 9.6 GHz) pulse EPR spectroscopy was performed on a CIQTEK EPR100 spectrometer. The length of π pulse was fixed to be 32 ns for all experiments, determined by nutation experiments.

Inversion recovery measurements: The spin-lattice relaxation time (T_1) was measured using an inversion recovery sequence $\pi - T - \pi/2 - \tau - \pi - \tau - echo$. For all experiments, a four-step phase cycling was employed with pulse phases of $(+x, -x, +x)$, $(+x, +x, +x)$, $(-x, -x, +x)$, and $(-x, +x, +x)$. The resulting echo decay was measured by varying the interval T , and the inversion recovery curve was fitted with a stretched exponential decay function for $(PPh_4)_2[Cu(mnt)_2]$ or a double-exponential decay function for COF-5 to extract T_1 .

Hahn echo decay measurements: T_2^{Hahn} was characterized using Hahn echo pulse sequence $(\pi/2 - \tau - \pi - \tau - echo)$. Two-step phase cycling was used to cancel baseline drift. The Hahn echo decay was measured by varying the interval τ , and the echo decay curve was fitted with a stretched exponential decay function for $(PPh_4)_2[Cu(mnt)_2]$ or a mono-exponential decay function for COF-5 to extract T_2 .

CPMG measurements: Typical CPMG sequence can be represented as $(\pi_x/2 - [\tau - \pi_y - 2\tau - \pi_y - \tau]_n - echo)$. We conducted two types of CPMG experiments. In the first type, while fixing pulse intervals ($\tau = 120, 150, 400$ ns for NV centers, $(PPh_4)_2[Cu(mnt)_2]$, and COF-5 respectively) and adding pulse number, the echo at time τ after each pulse was collected. In the second type, while fixing the pulse number and increasing the pulse interval, we monitored the decay of the echo at time τ after the last pulse, which can be fitted by a mono-exponential decay function to extract T_2 .

UDD measurements: For UDD- m , the inversion pulses were applied at time $t_n = t \sin^2 \frac{n\pi}{2(m+1)}$, $n = 1, 2, \dots, m$. The desired echo appeared at time t . Similar to CPMG experiments, we also conducted

two types of UDD- m experiments. In the first type, while fixing $t = 5000$ ns and adding pulse number, the desired echo after each pulse was collected. In the second type, while fixing the pulse number and increasing t , the decay curve of the desired echo after the last pulse was collected and fitted by a mono-exponential decay function to extract T_2 .

Optical detected magnetic resonance spectroscopy

Experiments for NV centers in diamond were performed with a homebuilt standard setup under a quantizing magnetic field of approximately 315 G, with microwave phase errors less than 1 degree and frequency detuning less than 1.5 MHz. The mono-exponential decay function was used for fitting to extract T_1 and T_2 .

Effective state fidelity test

Quantum state tomography: As mentioned in supplementary text (see equation (S40)), $s_{x,y,z}^i$ are required for state reconstruction. To obtain these values, $\frac{\pi_{x,-y}}{2}$ pulses were applied before measurements for $s_{y,x}^i$. No extra pulse was needed to measure s_z^i .

Test on the trapped ion qubit: The tests involve CP- m and UDD- m . CP- m can be represented as $(\pi_x/2 - (\tau - \pi_x - \tau)_m - echo)$. For CP- m experiments, the τ value was fixed to be 50 μ s. For the UDD- m sequences, the t value was fixed to be 1200 μ s. TPC's results were obtained from an average of 2048 shots for each phase cycling step; HPC's results were obtained from an average of 256 shots for each phase cycling step.

Test on the superconducting qubit: For CP- m experiments, the τ value was fixed to be 250 ns. For the UDD- m sequences, the t value was fixed to be 100 μ s. HPC results were obtained from an average of 1024 shots for each phase cycling step. TPC results were obtained similarly. Considering that TPC involves only two phase cycling steps, we intentionally added redundant experiments to align with HPC's number of shots.

Results of the superconducting qubit: Regarding UDD- m , HPC preserves F^{eff} above 99.3% up to 16 inversion pulses, whereas TPC gives rise to significantly smaller values, with F^{eff} dropping to 97.3% for UDD-16 and 53.5% for UDD-64. We further deliberately introduced systematic error to each pulse. For CP- m with $\pi/28$ systematic error, HPC retains F^{eff} above 99.3% for $m = 2-128$, whereas TPC causes an oscillation of F^{eff} , which drops to 0 for m being 32 and 96. Therefore,

HPC maintains remarkable robustness even under relatively large systematic error.

Supplementary Text

Problem setup

We consider a two-level quantum system (qubit) subject to pure dephasing errors. Without loss of generality, one can imagine it as an ensemble of electron spins ($S = \frac{1}{2}$) under a static and strong quantizing magnetic field B_0 along the z -axis, with pure dephasing errors described by the on-site disorder:

$$H = (\omega + \delta\omega_i(t))\hat{S}_z, \quad (\text{S1})$$

where $\delta\omega_i(t) \ll \omega$ and $\omega = g_e\mu_B\hbar^{-1}B_0$ is unperturbed Zeeman splitting with g_e , μ_B , \hbar , \hat{S}_z representing the g -factor of the electron spin, Bohr magneton, reduced Planck constant, and a Pauli- z matrix, respectively. We further assume that all spin-spin interaction terms are negligible such that \hat{S}_z is the only non-trivial term.

Due to the negligible spin-spin interactions, we focus on a single spin in the rotating frame for our analysis, where the first term $\omega\hat{S}_z$ can be omitted. The system's state is fully described by the 2×2 density matrix ρ . We assume the initial state to be:

$$\rho(0) = \begin{pmatrix} 1 & 0 \\ 0 & 0 \end{pmatrix}. \quad (\text{S2})$$

In general, the qubit's density matrix reads:

$$\rho = \begin{pmatrix} P_0 & C_+ \\ C_- & P_1 \end{pmatrix}, \quad (\text{S3})$$

where

- P_0 and P_1 represent populations of states $|0\rangle$ and $|1\rangle$, respectively, with $P_0 = 1 - P_1$;
- C_+ and C_- are complex conjugates ($C_- = C_+^*$) encoding the coherence between $|0\rangle$ and $|1\rangle$.

To understand why coherence-population mixing matters, we add longitudinal relaxation characterized by T_1 and transverse relaxation characterized by T_2 :

$$\rho(t) = \begin{pmatrix} 1 - P_1 e^{-t/T_1} & C_+ e^{-i\delta\omega t} e^{-t/T_2} \\ C_- e^{i\delta\omega t} e^{-t/T_2} & P_1 e^{-t/T_1} \end{pmatrix}. \quad (\text{S4})$$

Equivalently, the density matrix can be represented as:

$$\rho(t) = \frac{1}{2} [\hat{S}_0 + (1 - 2P_1 e^{-t/T_1}) \hat{S}_z + C_+ e^{-i\delta\omega t - t/T_2} \hat{S}_+ + C_- e^{i\delta\omega t - t/T_2} \hat{S}_-]. \quad (S5)$$

An ideal inversion pulse would exchange populations ($P_0 \leftrightarrow P_1$) and swap coherences ($C_+ \leftrightarrow C_-$) with a phase factor. However, imperfect (noisy) inversion pulses introduce coherence-population mixing, generating spurious signals like stimulated echoes that adversely affect coherence measurements.

The density matrix can be represented by a linear combination of a complete basis. The most commonly used basis set is $\{\hat{S}_0, \hat{S}_x, \hat{S}_y, \hat{S}_z\}$, where \hat{S}_0 is the two-dimensional identity matrix and $\hat{S}_{x,y,z}$ are Pauli matrices. Here, we choose $\{\hat{S}_0, \hat{S}_+, \hat{S}_-, \hat{S}_z\}$ because these terms explicitly represent coherence and population. It allows straightforward calculation of the free evolution with pure dephasing:

$$\begin{aligned} \hat{S}_0(t) &= \hat{S}_0(0), \\ \hat{S}_z(t) &= \hat{S}_z(0), \\ \hat{S}_+(t) &= \hat{S}_+(0) e^{-i\delta\omega t}, \\ \hat{S}_-(t) &= \hat{S}_-(0) e^{+i\delta\omega t}, \end{aligned} \quad (S6)$$

where $\hat{S}_\pm = \frac{1}{2}(\hat{S}_x \pm i\hat{S}_y)$. We can then define coherence orders $p = \pm 1, 0$:

$$\hat{S}_p(t) = \hat{S}_p(0) e^{-ip\delta\omega t}. \quad (S7)$$

Note that

$$\hat{S}_+ = \begin{pmatrix} 0 & 1 \\ 0 & 0 \end{pmatrix}, \hat{S}_- = \begin{pmatrix} 0 & 0 \\ 1 & 0 \end{pmatrix}, \frac{\hat{S}_0 + \hat{S}_z}{2} = \begin{pmatrix} 1 & 0 \\ 0 & 0 \end{pmatrix}, \frac{\hat{S}_0 - \hat{S}_z}{2} = \begin{pmatrix} 0 & 0 \\ 0 & 1 \end{pmatrix}. \quad (S8)$$

Evidently, $p = \pm 1$ represent coherence, and $p = 0$ represents population (see equation (S3)). For simplicity, we drop the identity term in the following analysis.

Hahn echo

The above basis enables calculation of the most well-known spin echo, namely Hahn echo, generated by a $\pi/2$ pulse followed by an inversion pulse (π pulse):

$$\hat{S}_z \xrightarrow{(\frac{\pi}{2})_y} \frac{\hat{S}_+ + \hat{S}_-}{2} \xrightarrow{\tau} \frac{\hat{S}_+ e^{-i\delta\omega\tau} + \hat{S}_- e^{i\delta\omega\tau}}{2} \xrightarrow{(\pi)_x} \frac{\hat{S}_- e^{-i\delta\omega\tau} + \hat{S}_+ e^{i\delta\omega\tau}}{2} \quad (S9)$$

After another free evolution time τ , $\frac{\hat{S}_+ + \hat{S}_-}{2}$ reappears, resulting in a Hahn echo. This echo reflects decoherence as it only involves $p = +1$ and $p = -1$ after the $\pi/2$ pulse. Note that $\delta\omega$ is assumed to be constant within time 2τ , and we apply this assumption throughout the following analysis for simplicity. We can also track the coherence order transfer during this process. There are two symmetric pathways: $0 \rightarrow +1 \rightarrow -1$ and $0 \rightarrow -1 \rightarrow +1$. Due to symmetry, we only need to consider one of them as \hat{S}_+ and \hat{S}_- always appear in pairs with equal magnitude.

Conclusion 1: Echo formation condition

The coherence order of the initial state is $p = 0$ according to equation (S2) and equation (S7). We can then represent the coherence transfer pathways by two series of coherence orders:

$$(0, p_1, p_2, \dots, p_n, -1), (0, -p_1, -p_2, \dots, -p_n, +1). \quad (\text{S10})$$

They are symmetric and essentially summarize the same dynamics. The echo formation condition requires the qubit to spend equal time in \hat{S}_+ and \hat{S}_- because all dephasing will be refocused by the inversion pulse according to equation (S6).

For free evolution times $(\tau_1, \tau_2, \dots, \tau_n)$ corresponding to each coherence order, if the final coherence order is -1 , the echo occurs at time t after the last pulse when the following condition is satisfied:

$$t = \sum_{i=1}^n p_i \tau_i > 0. \quad (\text{S11})$$

This means that the qubit spends more time on $p = +1$ than $p = -1$, so that it needs some extra time on $p = -1$ to form an echo. If the final coherence order is $+1$, then t has to be smaller than 0. Assume that the qubit has evolved according to the first coherence transfer pathway in equation (S10). It gains a phase of $e^{-i\delta\omega \sum_{i=1}^n p_i \tau_i} = e^{-i\delta\omega t}$. After free evolution time t on $p = -1$, this extra phase disappears according to equation (S6), generating an echo.

Stimulated echo

The classic pulse sequence generating a stimulated echo is: $(\frac{\pi}{2} - \tau - \frac{\pi}{2} - T - \frac{\pi}{2})$. While there exist numerous coherence transfer pathways, Conclusion 1 immediately reveals that a stimulated echo will appear at time τ after the last pulse, corresponding to the pathway $(0, +1, 0, -1)$ or

(0, -1, 0, +1). Pathways that do not form echoes (anti-echoes) are typically much weaker due to decoherence. The formation of stimulated echo involves coherence-population mixing after each pulse, so the dynamics of this echo reflects both decoherence and longitudinal relaxation.

Conclusion 2: Phase shift of signal

Note the i^{th} pulse induces a change in the coherence order Δp_i , and a phase change $\Delta \phi_i$ in the i^{th} pulse causes a phase shift in the final signal. Accordingly, the total phase shift $\Delta \Phi$ in the final signal is:

$$\Delta \Phi = \sum_i \Delta p_i \Delta \phi_i. \quad (\text{S12})$$

In this context, all phases are defined as the angle with respect to $+x$ axis. For example, a pulse along $+y$ has a $\frac{\pi}{2}$ phase, and the corresponding single qubit rotation is along $+y$ axis. An echo with phase $+y$ means the echo appears at $+y$ axis. In our setup, $\Delta p \in \{0, \pm 1, \pm 2\}$ and $\Delta \phi \in \{0, \pi\}$. This implies that changing a pulse's phase introduces a π phase shift to the final signal only when $\Delta p = \pm 1$. The coherence transfer pathways can thus be classified by the number of $\Delta p = \pm 1$ transitions. This classification aligns perfectly with our goal of distinguishing population and coherence. For k phase-flipped pulses:

- Even k : No change in the final signal ($\Delta \Phi = 0$)
- Odd k : Final signal gains a minus sign (π phase shift, i.e. $\Delta \Phi = \pi$)

These properties form the foundation of phase cycling design for inversion-pulse-based dynamical decoupling (IDD).

Phase cycling

Phase cycling enables selection of desired coherence transfer pathways and corresponding echoes. A noisy pulse could cause all possible coherence order transfers, and an N -pulse sequence can possibly generate $\frac{1}{2}(3^{N-1} - 1)$ echoes, making the phase cycling of dynamical decoupling sequences complicated.

Take CPMG- m sequence as an example, which includes a $\pi/2$ pulse followed by m spin-locking inversion pulses with equal intermittent free evolution times. We first consider the CPMG-2

sequence with fixed final coherence order $p = -1$ to show the principle of phase cycling. There are 4 coherence transfer pathways that could generate echoes after the last pulse as summarized in Table S1.

The desired pathway $(0, -1, +1, -1)$ representing qubit coherence overlaps with $(0, +1, 0, -1)$ (stimulated echo). Phase cycling resolves this issue: the desired echo is an one-pulse echo while the stimulated echo is a three-pulse echo, distinguished by the number of $\Delta p = \pm 1$ transitions within their pathways (Table S2). Later we will see such a classification allows us to analyze $\frac{1}{2}(3^{N-1} - 1)$ echoes in an elegant way. In this case, by performing two experiments, where one of them flips either inversion pulse with respect to the other experiment, and summing the final signals, the stimulated echo cancels out while the desired echo doubles (see Table S3 for a more complex phase cycling that involve four experiments).

Phase cycling problem in CPMG

Recall that a coherence transfer pathway can be represented as:

$$(0, p_1, p_2, \dots, p_{m+1}, -1).$$

The key to designing the phase cycling for CPMG- m is to exclude $p_i = 0$ within the coherence transfer pathway because we should probe pure decoherence processes ($p_i = \pm 1$) without involving the longitudinal relaxation. Our objective then reduces to eliminating $\Delta p = \pm 1$ transitions, which are generated by imperfect inversion pulses, except for the first $\pi/2$ pulse that prepares the coherence.

Consider the stimulated echo in the example of phase cycling in Table 3. Denote the original pulse phases (the first row) to be $[+1, +1, +1]$. These pulses produce the final signal with the original phase. Phase flipping of any pulse ($+1$ to -1 , i.e. $\Delta\phi_i = \pi$) inverts the signal sign, producing a π phase shift of the final signal. Critically, the phase of the final signal is determined by the product of all pulse phases. For instance:

- $[+1, +1, -1]$ and $[+1, -1, +1]$ yield the final signal with a π phase shift;
- $[+1, -1, -1]$ gives the final signal with the original phase.

Denote the original and π phase-shifted signals as $+1$ and -1 , respectively. The sum of results of the four phase cycling steps is $+1 + (-1) + (-1) + 1 = 0$, confirming that the phase cycling cancels

out the three-pulse echo, i.e. stimulated echo. In contrast, the desired echo is amplified because the phase of the first $\pi/2$ pulse is not flipped. Consequently, we can transform the design principle of phase cycling into an orthogonality condition that is concisely expressed as:

$$\begin{pmatrix} +1 \\ +1 \\ +1 \\ +1 \end{pmatrix} \circ \begin{pmatrix} +1 \\ +1 \\ -1 \\ -1 \end{pmatrix} \circ \begin{pmatrix} +1 \\ -1 \\ +1 \\ -1 \end{pmatrix} = \begin{pmatrix} +1 \\ -1 \\ -1 \\ +1 \end{pmatrix}. \quad (\text{S13})$$

Here, “ \circ ” denotes the Hadamard product, i.e. the element-wise product. The orthogonality requires the summation of all elements in the result vector to be zero. In this case, three-vector orthogonality translates to the cancellation of the three-pulse echo. As the phase of the desired echo is exclusively determined by the the phase of the first $\pi/2$ pulse, this orthogonality condition is applicable to all IDD sequences.

Basic definitions for phase cycling

Define a phase cycling set:

$$G \subseteq V_N, \quad G = \{g_1, g_2, \dots, g_n\} \cup \{E\} \quad (\text{S14})$$

where V_N is an N -dimensional vector space, each g_i contains equal numbers of $+1$ and -1 elements, and E is an all-one vector. The phase cycling matrix comprises elements from this set that are used as column vectors. Each row of this matrix represents phases of all pulses within the sequence in one phase cycling step, and each column represents the phase configuration of one pulse throughout all phase cycling steps.

Define Hadamard product orthogonality (HPO) of k column vectors in G if they fulfill the following condition:

$$g_1 \circ g_2 \circ \dots \circ g_k = g_i \neq E. \quad (\text{S15})$$

As the sum of all elements in g_i is equal to 0, this condition leads to the cancellation of k -pulse echoes.

Complete phase cycling (CPC)

Construction: We now prove that CPC for IDD- m , where m represents the number of inversion pulses, is possible by giving one construction directly. By definition, CPC mitigates all control errors—it cancels all k -pulse echoes for any $1 \leq k \leq m$, except for the desired echo. It is equivalent to constructing a matrix in which any subset of column vectors satisfies HPO. At present, we assume that the first $\pi/2$ pulse's phase is always +1 and focus on inversion pulses.

We construct a matrix encompassing all phase configurations of m inversion pulses. Each pulse has two phase choices, ± 1 . Accordingly, the matrix shape is $(2^m, m)$. This matrix can be represented as:

$$M = \{g_1, g_2, g_3, \dots, g_m\}. \quad (\text{S16})$$

We can easily check that any subset $K = \{g_{k_1}, g_{k_2}, \dots, g_{k_k}\}$ of M satisfies HPO, which requires half elements of the result vector $g_i = g_{k_1} \circ g_{k_2} \circ \dots \circ g_{k_k}$ equal to +1. Denote the number of +1 as $N(+1)$ and the number of -1 as $N(-1)$. The k vectors give rise to 2^k phase configurations, which are repeated 2^{m-k} times in the subset K . Therefore, we only need to consider one of the repetitions. Imagine k pulses whose phases are all initially +1. We can choose $0 \leq j \leq k$ of them to become -1, which gives rise to 2^k possible constructions of row vectors of the subset K . If we chose an even number of the original row to become -1, the product of all elements within the resulting row would be +1. If we chose an odd number of the original row to become -1, the product would be -1. We thus have:

$$\begin{aligned} N(+1) &= \sum_{\text{even}} C_k^{\text{even}}, \\ N(-1) &= \sum_{\text{odd}} C_k^{\text{odd}}. \end{aligned} \quad (\text{S17})$$

$N(+1)$ equals to $N(-1)$ because:

$$\begin{aligned} (-1 + 1)^k &= C_k^0(-1)^k + C_k^1(-1)^{k-1} + \dots + C_k^k(-1)^0 \\ &= \left(\sum_{\text{even}} C_k^{\text{even}} - \sum_{\text{odd}} C_k^{\text{odd}} \right) (-1)^k = 0 \end{aligned} \quad (\text{S18})$$

Therefore, any subset of M satisfies HPO. Namely, M represents CPC.

Complexity: While theoretically elegant, CPC becomes impractical for large m , requiring 2^m experiments. We prove that this is the minimal requirement.

Assume that M' is a CPC matrix (N, m) consisting of $\{g_1, g_2, \dots, g_m\}$. For any $i \neq j$, $g_i \circ g_j \notin M'$, because if $g_i \circ g_j = g_k \in M'$, then $g_i \circ g_j \circ g_k = g_k \circ g_k = E$, which is inconsistent with the property of CPC. Hence, $g_i \circ g_j$ results in a new element. It is orthogonal to any element in M' because $g_k \circ g_i = g_j$, $g_k \circ g_j = g_i$, and g_k and any other element in M' must fulfill HPO according to the property of CPC. We can construct C_m^2 such new elements. Similarly, they are orthogonal to each other. All new elements plus the original M' form a matrix whose all column vectors are mutually orthogonal. For same reasons, we can also group 3, 4, \dots , m elements together, and finally construct a much bigger matrix whose number of columns is:

$$C_m^1 + C_m^2 + C_m^3 + \dots + C_m^m = (1 + 1)^m - C_m^0 = 2^m - 1 \quad (\text{S19})$$

Note that we can always add E as the first column of the matrix, so finally we have 2^m elements. At this point, all the elements are still mutually orthogonal; equivalently, they are linearly independent. Therefore, the number of rows of the matrix (dimension of the present vector space) must be larger than or equal to the number of columns (dimension of the set of linearly independent vectors). Finally, we have:

$$N \geq 2^m. \quad (\text{S20})$$

The complexity of CPC is at least 2^m . The construction of CPC in Section 2.2.1 is optimal.

Experimental Consideration: While theoretically setting the first pulse's phase to E suffices, practical implementations often phase cycling the first pulse as $\begin{pmatrix} E \\ -E \end{pmatrix}$ to eliminate baseline drift.

This is actually a combination of CPC and two-step phase cycling (TPC). Fortunately, we can now set the first inversion pulse's phase to be E because it does not cause any unwanted signal if we neglect anti-echoes. So, the complexity is still 2^m .

Two-step phase cycling: TPC involves two quantum circuits that differ only in phase of the first $\pi/2$ pulse; one uses a $\pi_x/2$ pulse and the other uses $\pi_{-x}/2$ pulse. Subtracting the results of these two circuits effectively cancels baseline drift. For experiments on single trapped ion, superconducting qubits, and NV centers in diamond, an extra $\pi/2$ pulse is applied before measuring population distribution. In this case, phase cycling the final $\pi/2$ pulse also suffices.

Hadamard phase cycling (HPC)

Since CPC has exponential complexity $O(2^m)$, it is meaningful to design a good approximate phase cycling matrix that eliminates as many unwanted signals as possible while maintaining as low complexity as possible. Here, we show that regarding IDD- m sequences, HPC has only linear complexity $O(m)$ while canceling out more than 98% unwanted signals for $m > 16$.

Sylvester's construction of Hadamard matrix: Hadamard matrix is a square matrix of elements $+1$ and -1 , where any two columns of the matrix are orthogonal: $H^T H = nI$. Mathematicians suspect that any Hadamard matrix of order $4n$ always exists, where n is an integer. This Hadamard conjecture remains unproved, but there exist many methods to construct Hadamard matrix. Here, we use Sylvester's method to construct Hadamard matrix of order 2^n :

$$H_{2^n} = \begin{pmatrix} H_{2^{n-1}} & H_{2^{n-1}} \\ H_{2^{n-1}} & -H_{2^{n-1}} \end{pmatrix}, H_1 = \begin{pmatrix} 1 \end{pmatrix}. \quad (\text{S21})$$

Note that this matrix's first column is always an all-one vector, and due to its original orthogonality, it automatically mitigates all stimulated echoes that overlap with the desired echoes of CPMG.

Phase cycling group

Represent Sylvester's Hadamard matrix as $H = \{E, g_1, g_2, \dots, g_H\}$ like previous discussions. This set is an abelian group under Hadamard product, resulting in great HPO that means although not all subsets of the phase cycling matrix satisfy HPO, a significantly large ratio of subsets do satisfy.

Note that an abelian group requires the elements to satisfy these five properties:

Closure: $\forall g_i, g_j \in H; g_i \circ g_j \in H$.

Identity Existence: $\forall g, \exists E; g \circ E = E \circ g = g$.

Inverse Existence: $\forall g, \exists g^{-1}; g \circ g^{-1} = g^{-1} \circ g = E$.

Associative law: $\forall g_i, g_j, g_k \in H, (g_i \circ g_j) \circ g_k = g_i \circ (g_j \circ g_k)$.

Commutative law: $\forall g_i, g_j \in H, g_i \circ g_j = g_j \circ g_i$.

Hadamard product is essentially a multiplication, so it automatically satisfies the associative law and the commutative law. The identity in H is E , which consists of only $+1$ elements. The inverse of an element is just itself. Here, we prove the closure of H . First, notice that H_2 obviously satisfies the closure. Based on the Sylvester's construction of H_4 from H_2 , the new elements in

H_4 also satisfy the closure because they are formed by stacking elements in H_2 . Similar logic is applicable to any higher-order matrix. In fact, one can treat $\begin{pmatrix} H & H \\ H & -H \end{pmatrix}$ as some kind of H_2 , then the closure becomes obvious.

$$H_2 = \begin{pmatrix} 1 & 1 \\ 1 & -1 \end{pmatrix}, H_4 = \begin{pmatrix} 1 & 1 & 1 & 1 \\ 1 & -1 & 1 & -1 \\ 1 & 1 & -1 & -1 \\ 1 & -1 & -1 & 1 \end{pmatrix}. \quad (\text{S22})$$

Great Hadamard product orthogonality

We now prove the great HPO of the phase cycling group. We first prove a conclusion to give some intuitions of the phase cycling group's great HPO:

$$\begin{aligned} g_1 \circ g_2 \circ \cdots \circ g_{i-1} \circ g_i &= E \\ g_1 \circ g_2 \circ \cdots \circ g_{i-1} &= E \circ g_i \\ g_1 \circ g_2 \circ \cdots \circ g_{i-1} \circ g_j &= E \circ g_i \circ g_j \\ g_i \circ g_j &= g_k \neq E \end{aligned} \quad (\text{S23})$$

Accordingly, if we had i elements that do not satisfy HPO, we would be able to change any one of them to another element beyond the original set to construct a new set whose elements satisfy HPO.

We now discuss the proportion of the number of combinations of elements that do not satisfy HPO. Assume that we have 2^n elements in the phase cycling group G_H , and pick q elements from $G_H - \{E\}$. Define $p(q)$ as the probability that these elements do not satisfy HPO, and define $D(q)$ as the number of combinations satisfying $g_1 \circ g_2 \cdots \circ g_q = E$, where $1 \leq q \leq 2^n - 1$. We have:

$$p(q) = \frac{D(q)}{C_{2^n-1}^q}. \quad (\text{S24})$$

Due to the definition of G_H , $p(1) = p(2) = 0$.

When $q = 3$, we need the three elements to satisfy $g_3 = g_1 \circ g_2 \neq E$. Given two elements, then the third element is uniquely determined. However, there are double counting issues while choosing the third element (we have to determine which one of the three elements is the third

element), finally:

$$D(3) = \frac{C_{2^n-1}^2}{C_3^1}. \quad (\text{S25})$$

When $q = 4$, we need the elements to satisfy $g_4 = g_1 \circ g_2 \circ g_3 \neq E$. Again, given three elements, the fourth element is uniquely determined. Moreover, we have to subtract $D(3)$ combinations satisfying $g_1 \circ g_2 \circ g_3 = E$, because in this case, g_4 would have to be E to satisfy our requirement, which is impossible. Taking the double counting issue into account, we have:

$$D(4) = \frac{C_{2^n-1}^3 - D(3)}{C_4^1}. \quad (\text{S26})$$

When $q = 5$, we need the elements to satisfy $g_5 = g_1 \circ g_2 \circ g_3 \circ g_4 \neq E$. Again, given four elements, the fifth element is uniquely determined. Furthermore, we have to subtract combinations satisfying $g_1 \circ g_2 \circ g_3 \circ g_4 = E$ for same reasons as $q = 4$ case. In addition, when $g_1 \circ g_2 \circ g_3 \circ g_4 \neq E$, we need to subtract combinations satisfying $g_1 \circ g_2 \circ g_3 = E$ because this leads to an impossible relation, $g_4 \circ g_5 = E$. Similarly, we have $D(4)$ combinations for the former one. For the latter one, we have $D(3)$ combinations for g_1, g_2, g_3 , and $2^n - 1 - 3$ choices for the fourth elements. Finally:

$$D(5) = \frac{C_{2^n-1}^4 - D(4) - (2^n - 1 - 3)D(3)}{C_5^1}. \quad (\text{S27})$$

In fact, the situation of $q = 5$ includes all necessary conditions. Hence, we can consider the general case, i.e. $q \geq 5$ elements satisfying $g_1 \circ g_2 \circ \dots \circ g_q = E$. Given $q - 1$ elements, we need to subtract $D(q - 1)$ combinations for $g_1 \circ g_2 \circ \dots \circ g_{q-1} = E$, and then subtract $(2^n - 1 - q + 2)D(q - 2)$ combinations for $g_1 \circ g_2 \circ \dots \circ g_{q-2} = E$. We thus have:

$$D(q) = \frac{C_{2^n-1}^{q-1} - D(q-1) - (2^n - q + 1)D(q-2)}{C_q^1}, \quad (\text{S28})$$

$$p(q) = \frac{1 - p(q-1) - (q-1)p(q-2)}{2^n - q}.$$

It is straightforward to check that only $q = 1$ violates this relation, but it is a trivial case with $D(1) = p(1) = 0$. Besides, $D(q) = D(2^n - 1 - q)$ because $g_1 \circ g_2 \circ \dots \circ g_{2^n-1} = E$.

We continue to derive the general formula for $D(q)$ and $p(q)$ based on the recursive formula. First, we prove a lemma:

$$p(2k) = p(2k - 1). \quad (\text{S29})$$

When $k = 1$, $p(2) = p(1) = 0$. When $k = l$, assume that $p(2l) = p(2l - 1)$. Hence, when $k = l + 1$, using equation (S28):

$$\begin{aligned} (2^n - 2l - 1) \times p(2l + 1) &= 1 - p(2l) - 2l \times p(2l - 1), \\ (2^n - 2l - 2) \times p(2l + 2) &= 1 - p(2l + 1) - (2l + 1) \times p(2l). \end{aligned} \quad (\text{S30})$$

From these equations, we get:

$$p(2(l + 1)) = p(2(l + 1) - 1). \quad (\text{S31})$$

We thus prove the lemma.

For $q = 2k + 1$:

$$\begin{aligned} D(2k + 1) &= \frac{C_{2^{n-1}}^{q-1} - D(q - 1) - (2^n - q + 1)D(q - 2)}{q} \\ &= \frac{C_{2^{n-1}}^{q-1}}{q} - \frac{(2^n - q + 1)D(q - 2)}{q - 1}. \end{aligned} \quad (\text{S32})$$

Write $\frac{C_{2^{n-1}}^{q-1}}{q}$ as $\frac{C_{2^{n-1}}^q}{2^n} + \frac{(2^n - q + 1)C_{2^{n-1}}^{q-2}}{(q-1)2^n}$, and change q to $2k + 1$:

$$D(2k + 1) - \frac{C_{2^{n-1}}^{2k+1}}{2^n} = -\frac{2^{n-1} - k}{k} \left[D(2k - 1) - \frac{C_{2^{n-1}}^{2k-1}}{2^n} \right]. \quad (\text{S33})$$

Use this relation and $D(1) = 0$, we finally get:

$$D(2k + 1) = \frac{C_{2^{n-1}}^{2k+1}}{2^n} + (-1)^{k+1} \times \frac{(2^n - 1)C_{2^{n-1}-1}^k}{2^n}. \quad (\text{S34})$$

Similarly:

$$D(2k) = \frac{C_{2^{n-1}}^{2k}}{2^n} + (-1)^k \times \frac{(2^n - 1)C_{2^{n-1}-1}^k}{2^n}. \quad (\text{S35})$$

For $p(q)$, we have:

$$\begin{aligned} p(2k) &= \frac{1}{2^n} + (-1)^k \times \frac{2^n - 1}{2^n} \times \frac{C_{2^{n-1}-1}^k}{C_{2^{n-1}}^{2k}}, \\ p(2k + 1) &= \frac{1}{2^n} + (-1)^{k+1} \times \frac{2^n - 1}{2^n} \times \frac{C_{2^{n-1}-1}^k}{C_{2^{n-1}}^{2k+1}}. \end{aligned} \quad (\text{S36})$$

Theoretically, for an IDD sequence with 32 inversion pulses, CPC requires $2^{32} = 4, 294, 967, 296$ steps, while the phase cycling based on Hadamard matrix only requires 32 steps. The HPO ratio, which is defined as $1 - \sum_k \frac{D(k)}{C_{2^{n-1}}^k}$, is 96.88%.

Final phase cycling scheme

We further improve the HPO ratio by harnessing the parity of coherence transfer pathways and TPC. Note that the Sylvester's Hadamard matrix has extra freedoms to create new Hadamard matrices. For example, if we change the first column from E to $-E$, the matrix is still a Hadamard matrix with great HPO. We can also add a minus sign to all the rest columns as well, i.e. changing $H' \rightarrow -H'$, to construct a new stacked Hadamard matrix:

$$\begin{pmatrix} E & H' \\ E & -H' \end{pmatrix}. \quad (\text{S37})$$

The advantage of this new matrix is that any odd number of elements excluding the first column satisfy HPO. Formally, if q is an odd number, $D(q) = 0$. Imagine that there are odd number of elements in H' forming an unwanted signal; namely, these elements do not satisfy HPO. The Hadamard product of these elements in $-H'$ has an opposite sign. Thus, adding these two Hadamard products together would satisfy HPO. Such stacking increases the HPO ratio from 96.88% to 98.44% for IDD-32. Finally, we can add a column for the first $\pi/2$ pulse to construct HPC:

$$\begin{pmatrix} + & E & E & H' \\ + & E & E & -H' \\ - & -E & E & H' \\ - & -E & E & -H' \end{pmatrix}. \quad (\text{S38})$$

Note that we do not need the first two columns to satisfy HPO if we neglect anti-echoes. For IDD- m , we need $4 \times N_{HPC}$ phase cycling steps, where $N_{HPC} = 2^{\text{integer}}$ is the smallest number satisfying $N_{HPC} \geq m$. For example, HPC needs 128 phase cycling steps for IDD-32, but it needs 256 phase cycling steps for IDD-34. In sharp contrast, CPC would need 4, 294, 967, 296 and 17, 179, 869, 184 steps for IDD-32 and IDD-34, respectively, both of which are clearly not practical.

Overall, whereas CPC has a complexity of $O(2^m)$ for IDD- m , HPC significantly reduces the complexity to $O(m)$ while preserving near-quantitative HPO ratio. HPC is both scalable and effective.

Effective State Fidelity

Definition: State fidelity serves as a merit of how close two quantum states are, which is typically defined as:

$$F(\rho, \sigma) = (\text{Tr} \sqrt{\sqrt{\rho} \sigma \sqrt{\rho}})^2. \quad (\text{S39})$$

Here, σ represents the target state and ρ the state for comparison. We define:

$$S_{x,y,z} = \sum_i V_s^i s_{x,y,z}^i$$

$$\langle S_{x,y,z} \rangle = \frac{S_{x,y,z}}{\sqrt{S_x^2 + S_y^2 + S_z^2}}, \quad (\text{S40})$$

where V_s^i is the i_{th} element of the sign vector (see equation (S38)) and $s_{x,y,z}^i$ are expectation values of Pauli operators for the i_{th} phase cycling step. We call $\langle S_{x,y,z} \rangle$ as phase-cycled expectation values and use them to reconstruct the effective quantum state:

$$\rho^{eff} = \frac{1}{2} (\hat{S}_0 + \langle S_x \rangle \hat{S}_x + \langle S_y \rangle \hat{S}_y + \langle S_z \rangle \hat{S}_z). \quad (\text{S41})$$

Finally, the effective state fidelity reads

$$F(\rho^{eff}, \sigma) = (\text{Tr} \sqrt{\sqrt{\rho^{eff}} \sigma \sqrt{\rho^{eff}}})^2. \quad (\text{S42})$$

The effective state fidelity serves as a useful benchmark for phase cycling. Essentially, phase cycling sums different Bloch vectors, which represent qubit states, to get a more accurate Bloch vector. Thus, the better the phase cycling method, the higher the effective state fidelity (if the DD sequence does not have inherent robustness).

Shortcomings of robust dynamical decoupling sequences: There are many robust IDD sequences that can fight against control errors, e.g. CPMG, XY-4, XY-8, etc. They share similar essence: compensating previous errors by following pulses. Ironically, such compensations efficiently cause coherence-population mixing. Below is an example of CPMG-2 with longitudinal and transverse relaxations but without dephasing, the latter of which is assumed to be eliminated by IDD. Imagining that we first create a coherence C_+ and let it evolve for time τ , we will get:

$$C_+(\tau) = C_+ e^{-\frac{\tau}{T_2}}. \quad (\text{S43})$$

Then we apply a noisy inversion pulse and consider these two terms:

$$\begin{aligned} C_+(\tau) &\rightarrow C'_-(\tau) = C'_- e^{-\frac{\tau}{T_2}}, \\ C_+(\tau) &\rightarrow P'_1(\tau) = P'_1 e^{-\frac{\tau}{T_2}}. \end{aligned} \tag{S44}$$

Again, let them evolve for 2τ :

$$\begin{aligned} C'_-(3\tau) &= C'_- e^{-\frac{3\tau}{T_2}}, \\ P'_1(3\tau) &= P'_1 e^{-\frac{\tau}{T_2}} e^{-\frac{2\tau}{T_1}}. \end{aligned} \tag{S45}$$

Then we apply another noisy inversion pulse, two possible terms are:

$$\begin{aligned} C'_-(3\tau) &\rightarrow C''_+(3\tau) = C''_+ e^{-\frac{3\tau}{T_2}}, \\ P'_1(3\tau) &\rightarrow C''_-(3\tau) = C''_- e^{-\frac{\tau}{T_2}} e^{-\frac{2\tau}{T_1}}. \end{aligned} \tag{S46}$$

In fact, the second term definitely exists for noisy circuits because the conversion from P_1 to C_- is exactly the compensation done by CPMG; namely, this term is the consequence of the robustness. These two processes correspond to $(0, +1, -1, +1)$ and $(0, +1, 0, -1)$ coherence transfer pathways. According to the Conclusion 1, each of them gives rise to an echo after another evolution time τ . The second process clearly introduces longitudinal relaxation into decoherence, resulting in an overestimation of T_2 .

This not only serves as a vivid example of how coherence-population mixing leads to slower decay of the apparent signal, but also points out long-standing yet overlooked shortcomings of robust IDD sequences. Although these sequences can use later pulses to correct previous control errors, these errors still leave influence on the history of dynamics, which possibly distorts tasks such as T_2 acquisition and quantum sensing. Therefore, a non-Markovian quantum error mitigation method is indispensable to correctly probe the intermediate dynamic processes. On the other hand, robust sequences remain useful when the target task does not require correct observation of the intermediate dynamic processes, or when the single-gate fidelity is sufficiently high.

Notably, the way of robust sequences to preserve state fidelity is different from phase cycling. The former only preserve the fidelity of the final state, whereas the latter protects the effective fidelity of every intermediate state. Although one may get a high state fidelity after a robust sequence, the measurement of T_2 may still be incorrect due to erroneous intermediate dynamics.

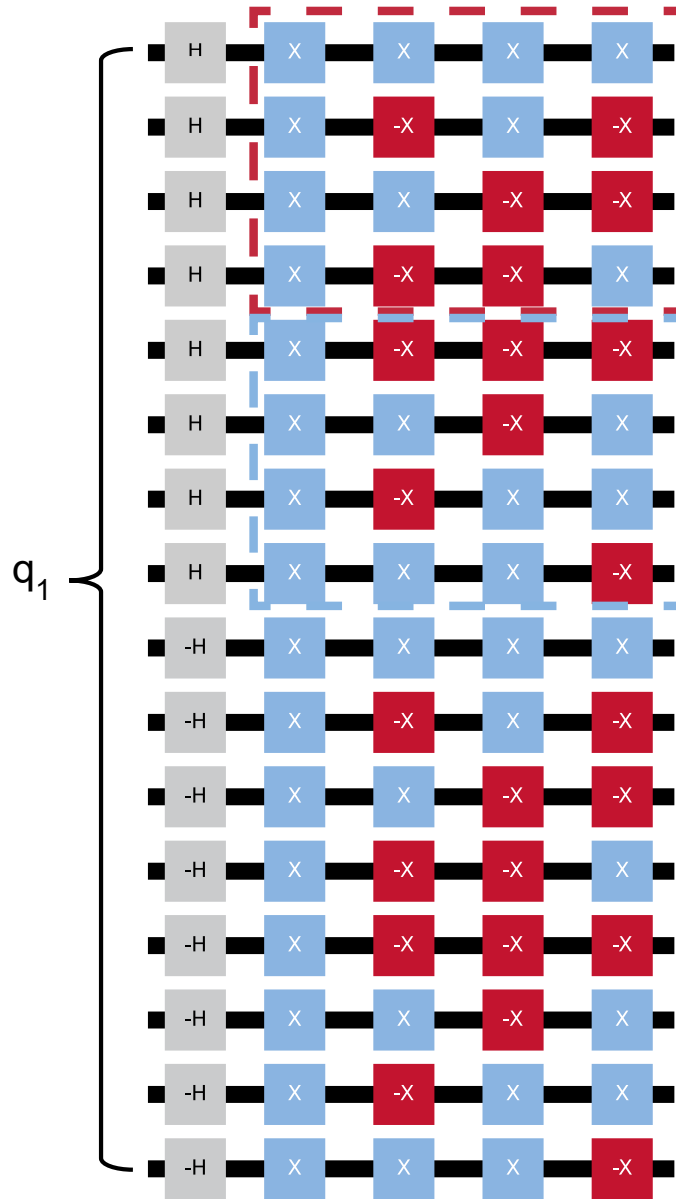


Figure S1: Hadamard phase cycling for IDD-4. q_1 and H represent qubit and Hadamard gate ($\pi/2$ gate), respectively. $\pm X$ represent inversion pulses with opposite phases. Phase configurations within red block represent the original Hadamard matrix, and phase configurations within blue block represent a minus Hadamard matrix except for the first column.

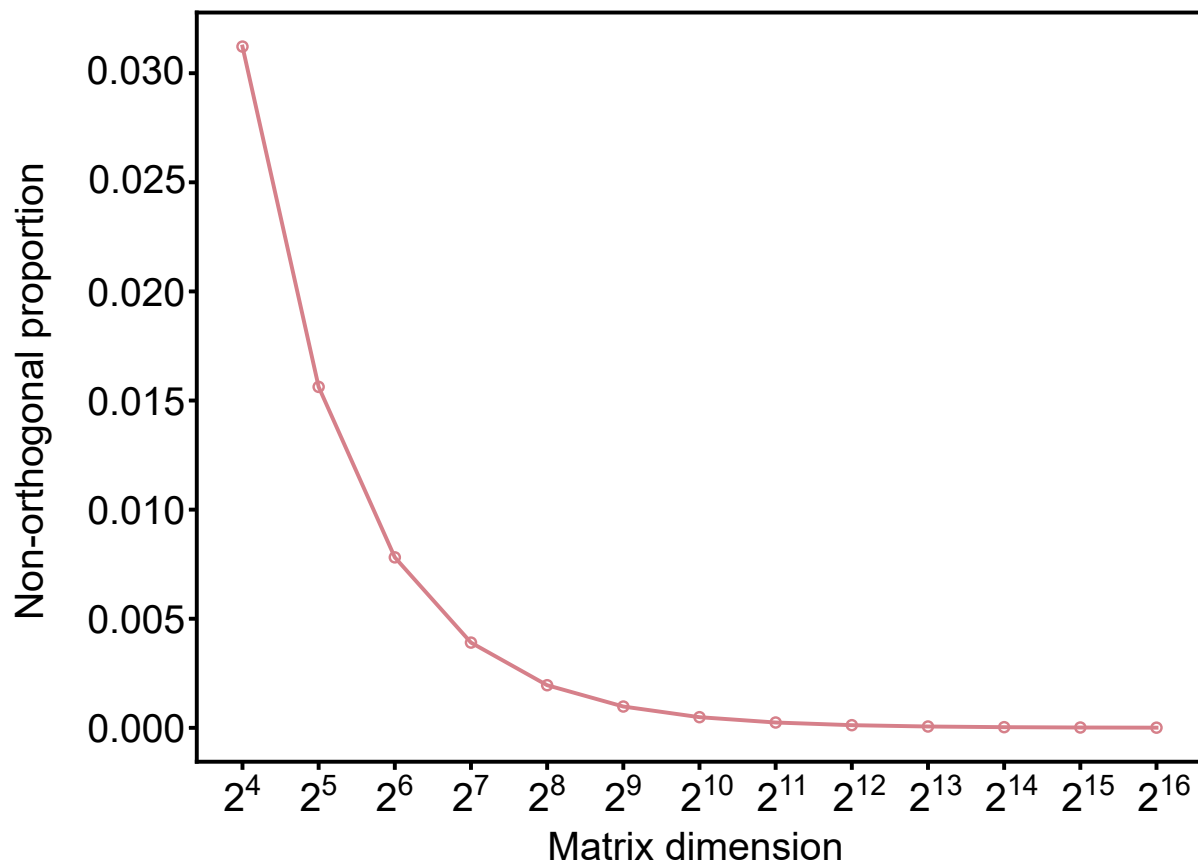


Figure S2: Pulse EPR spectroscopic characterization results of $(\text{PPh}_4)_2[\text{Cu}(\text{mnt})_2]$ at 8 K.
Non-orthogonal ratio (1-HPO ratio) of HPC with different dimensions of Hadamard matrices.

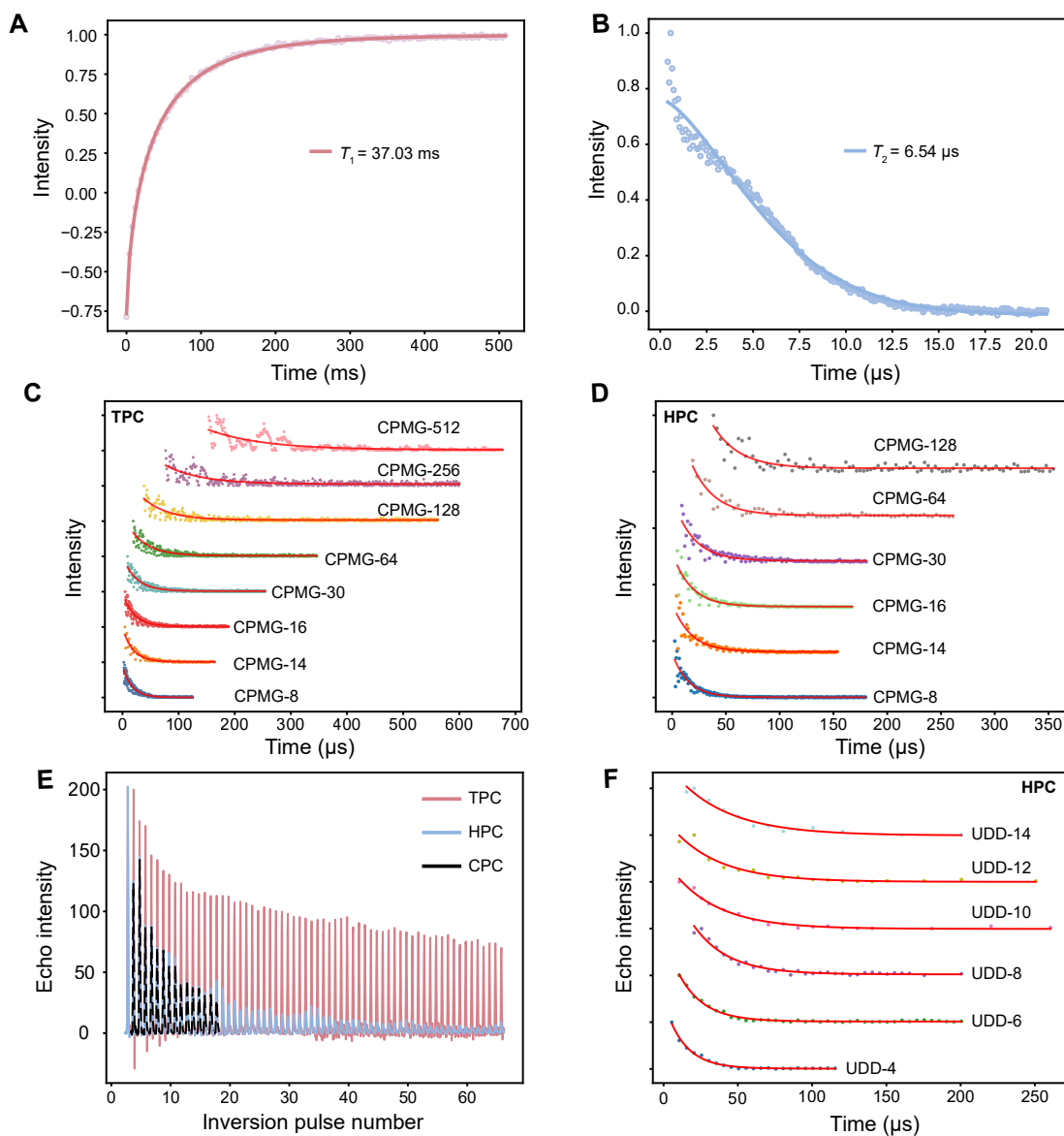


Figure S3: Pulse EPR spectroscopic characterization results of $(\text{PPh}_4)_2[\text{Cu}(\text{mnt})_2]$ at 8 K. **A**, inversion recovery curve. **B**, Hahn echo decay curve. **C,D**, echo decay curves for CPMG experiments with TPC and HPC, respectively. **E**, comparison between echoes collected under CPMG with different phase cycling methods. **F**, echo decay curves for UDD experiments with HPC.

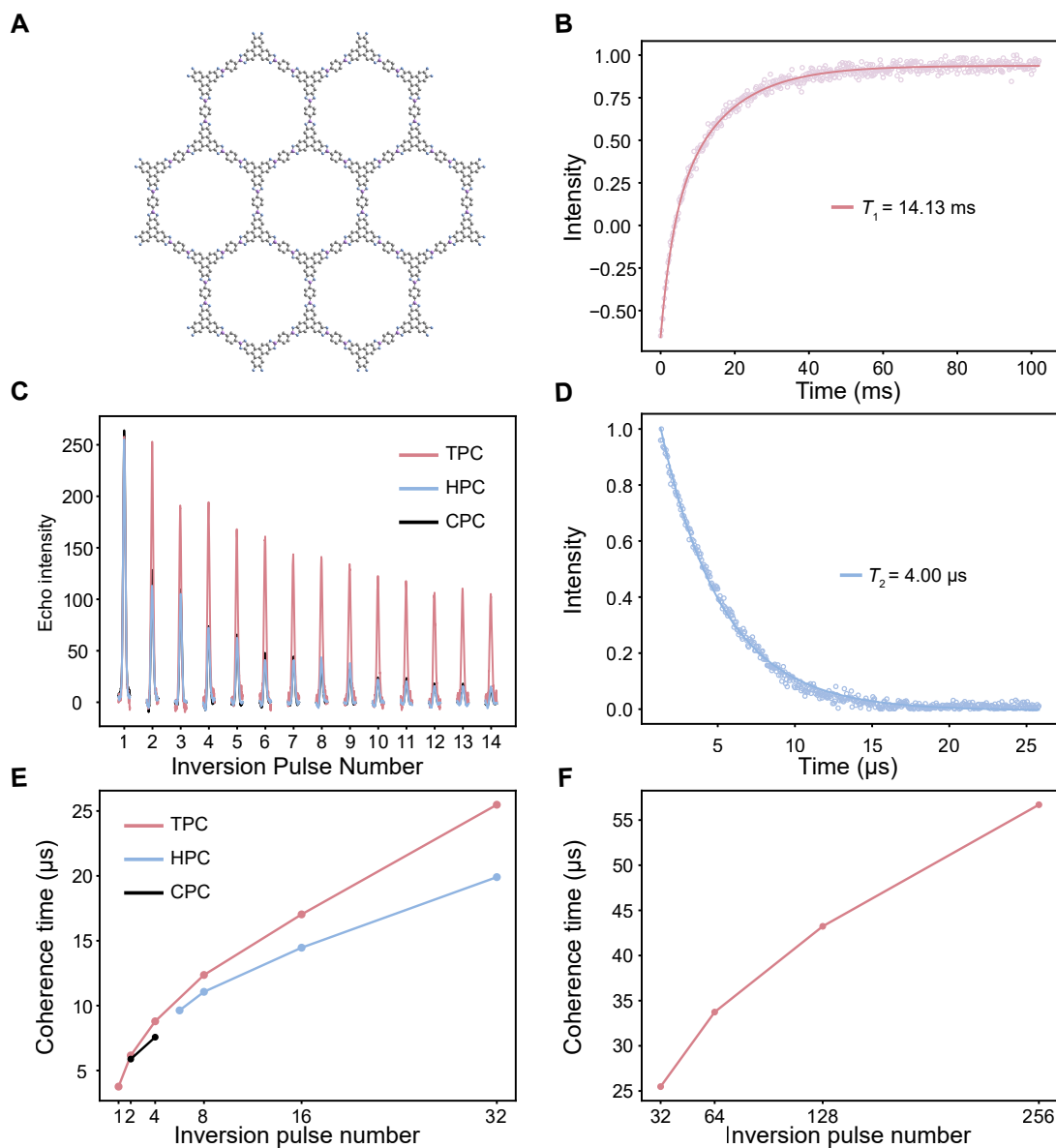


Figure S4: Pulse EPR spectroscopic characterization results of COF-5 at 80 K. **A**, structure of COF-5. **B**, inversion recovery curve. **C**, comparison between echoes collected under CPMG with different phase cycling methods. **D**, Hahn echo decay curve. **E**, comparison between T_2 measured by CPMG with different phase cycling methods. **F**, T_2 measured by CPMG with TPC.

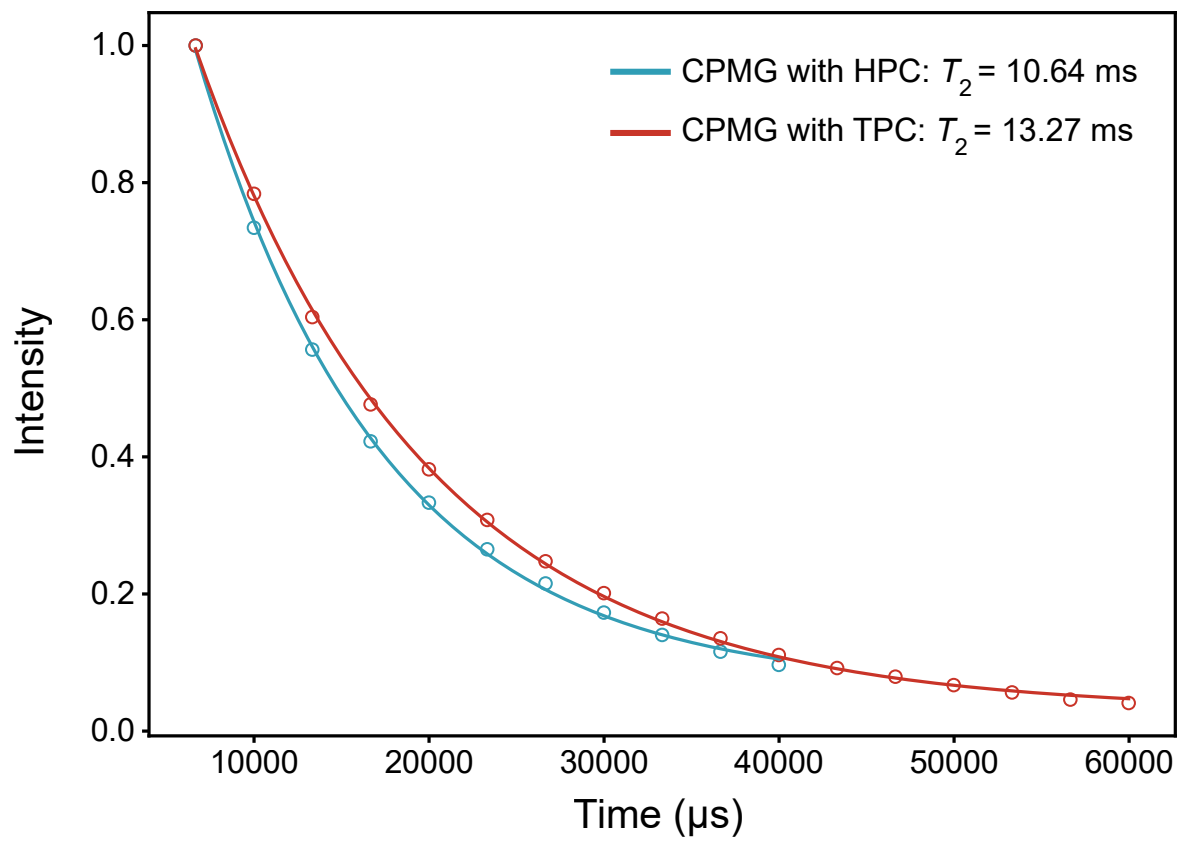


Figure S5: CPMG Results with different phase cycling methods of SSNMR.

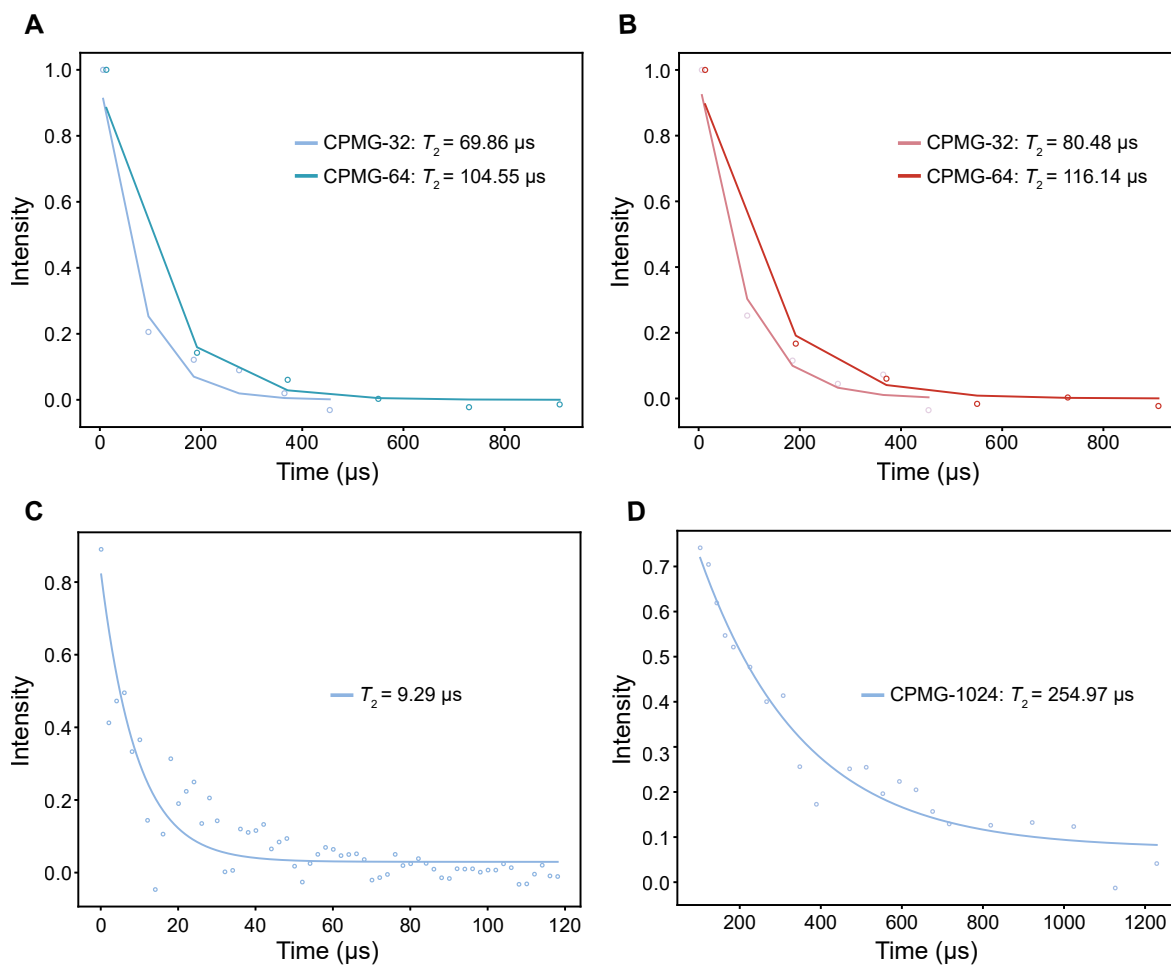


Figure S6: Optically detected magnetic resonance spectroscopic characterization results of diamond NV Centers. A,B, signal decay curves of CPMG-32 and CPMG-64 with HPC and TPC, respectively. **C,** Hahn echo decay curve. **D,** echo decay curve collected by CPMG-1024 with TPC.

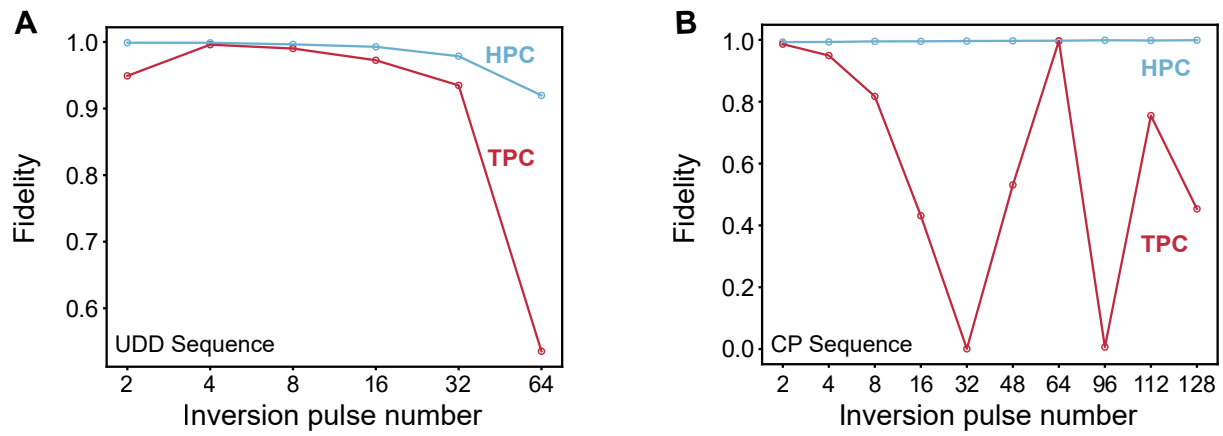


Figure S7: Effective state-fidelity tests on single superconducting transmon qubit. A, results for UDD experiments with TPC and HPC. **B,** results for CP experiments with TPC and HPC. A $\pi/28$ systematic error was introduced to each inversion pulse.

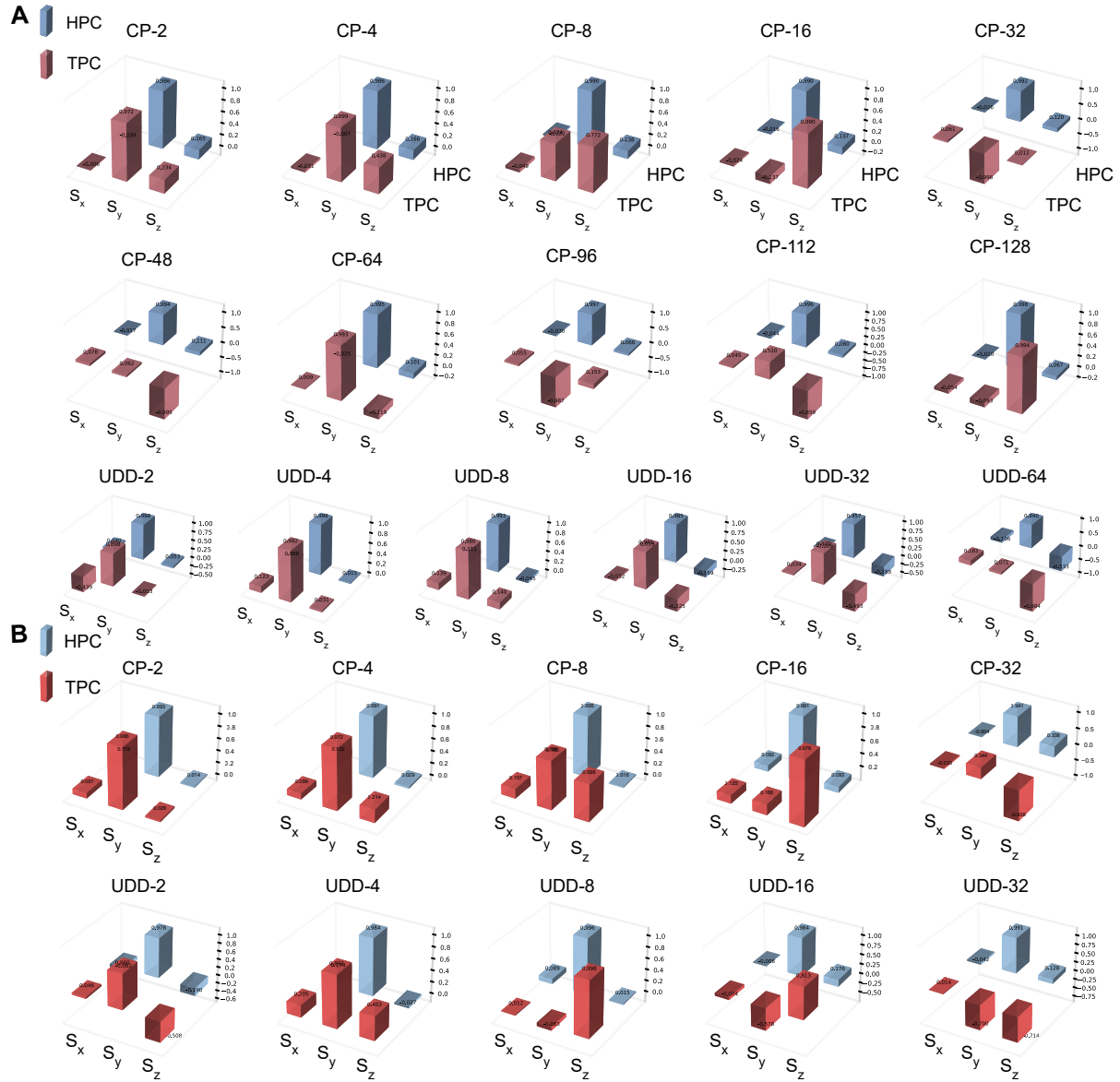


Figure S8: Quantum state tomography results. A, Single superconducting transmon qubit results and **B**, single trapped ion qubit results.

Table S1: Coherence transfer pathways in CPMG-2. Echo position is with respect to the last pulse.

p_0	p_1	p_2	p_3	Echo Position
0	-1	+1	-1	τ
0	+1	+1	-1	3τ
0	0	+1	-1	2τ
0	+1	0	-1	τ

Table S2: Changes of coherence orders in CPMG-2

Δp_0	Δp_1	Δp_2	Δp_3	Echo Position
<i>None</i>	-1	+2	-2	τ
<i>None</i>	+1	-1	-1	τ

Table S3: Complete phase cycling for CPMG-2. The symbol in the “Sign” column indicates addition or subtraction of the final signal. “Original” and “Flipped” represent phases of echoes.

Sign	Pulse 1	Pulse 2	Pulse 3	Desired echo	Stimulated Echo
+	+X	+Y	+Y	Original	Original
+	+X	+Y	-Y	Original	Flipped
+	+X	-Y	+Y	Original	Flipped
+	+X	-Y	-Y	Original	Original

Table S4: Example of CPC for CPMG-4. Note: Consider a subset $K = \{g_3, g_4\}$. Regarding the last two pulses, the first four rows already contain all possible phase configurations, and the rest of rows are simply their repetitions.

Pulse 1	Pulse 2	Pulse 3	Pulse 4
+	+	+	+
+	+	+	-
+	+	-	+
+	+	-	-
+	-	+	+
+	-	+	-
+	-	-	+
+	-	-	-
-	+	+	+
-	+	+	-
-	+	-	+
-	+	-	-
-	-	+	+
-	-	+	-
-	-	-	+
-	-	-	-

Table S5: T_2 of $(\text{PPh}_4)_2[\text{Cu}(\text{mnt})_2]$ under IDD-m.

m	Phase cycling	T_2 (μs)	IDD
8	HPC	14.85	CPMG
8	TPC	16.80	CPMG
14	HPC	17.17	CPMG
14	TPC	18.50	CPMG
16	HPC	17.39	CPMG
16	TPC	20.58	CPMG
30	HPC	18.80	CPMG
30	TPC	24.63	CPMG
64	HPC	21.13	CPMG
64	TPC	33.13	CPMG
128	HPC	24.42	CPMG
128	TPC	43.53	CPMG
256	TPC	64.05	CPMG
512	TPC	98.91	CPMG
4	HPC	13.70	UDD
6	HPC	16.88	UDD
8	HPC	23.22	UDD
10	HPC	30.56	UDD
12	HPC	31.56	UDD
14	HPC	35.72	UDD

Table S6: T_2 of COF-5 under IDD-m

m	Phase cycling	T_2 (μs)	IDD
2	CPC	5.88	CPMG
4	CPC	7.57	CPMG
6	HPC	9.63	CPMG
8	HPC	11.06	CPMG
16	HPC	14.47	CPMG
32	HPC	19.91	CPMG
2	TPC	6.16	CPMG
4	TPC	8.79	CPMG
8	TPC	12.36	CPMG
16	TPC	17.03	CPMG
32	TPC	25.48	CPMG
64	TPC	33.74	CPMG
128	TPC	43.23	CPMG
256	TPC	56.70	CPMG